Single bubble and drop techniques for characterizing foams and emulsions

V. Chandran Suja[a], M. Rodríguez-Hakim[a,b], J. Tajuelo[a,c], G.G. Fuller[a]

[a] *Department of Chemical Engineering, Stanford University, Stanford, California 94305, USA*
[b] *Department of Materials, ETH Zurich, Vladimir-Prelog-Weg 5, Zurich 8093, Switzerland*
[c] *Departamento de Física Interdisciplinar, Universidad Nacional de Eduación a Distancia UNED, Madrid 28040, Spain*

Abstract

The physics of foams and emulsions has traditionally been studied using bulk foam/emulsion tests and single film platforms such as the Scheludko cell. Recently there has been a renewed interest in a third class of techniques that we term as single bubble/drop tests, which employ isolated whole bubbles and drops to probe the characteristics of foams and emulsions. Single bubble and drop techniques provide a convenient framework for investigating a number of important characteristics of foams and emulsions, including the rheology, stabilization mechanisms, and rupture dynamics. In this review we provide a comprehensive discussion of the various single bubble/drop platforms and the associated experimental measurement protocols including the construction of coalescence time distributions, visualization of the thin film profiles and characterization of the interfacial rheological properties. Subsequently, we summarize the recent developments in foam and emulsion science with a focus on the results obtained through single bubble/drop techniques. We conclude the review by presenting important venues for future research.

Keywords: Foams, Emulsions, Thin film interferometry, Coalescence time distributions, Interfacial rheology

Contents

1 Introduction . . . 2
2 Historical Perspective . . . 3
3 Methods . . . 4
3.1 Single bubble and single drop setups . . . 4
3.2 Coalescence time distributions . . . 5
3.3 Thin film profile reconstruction . . . 7
3.4 Interfacial rheological properties . . . 9
3.4.1 Static and Dynamic Interfacial Stress . . . 9
3.4.2 Dilatational rheology . . . 13
4 Foam stability . . . 16
4.1 Foam Density . . . 16
4.2 Coalescence time distributions . . . 17
4.3 Stabilization Mechanisms . . . 18
4.4 Bubble rupture dynamics . . . 18
5 Emulsion stability . . . 19
5.1 Stabilization mechanisms and film rupture . . . 19
5.2 Single drop experimental approach . . . 20
5.2.1 Coalescence time distribution and drainage rate . . . 20
5.2.2 Drop rupture dynamics and retraction speed . . . 21
6 Conclusion and Outlook . . . 22
Appendix A Matlab Codes . . . 23
Appendix B Simple Emulsion/Foam Model . . . 23
Appendix C Cumulative Coalescence Time Distributions . . . 23
Appendix D Intensity of light reflected from a thin film . . . 24

1. Introduction

Foams and emulsions are dispersions of a gas and a liquid, respectively, in a different liquid. Foams are common and desirable in a number of applications such as food manufacturing processes, personal and health care product development, detergency, firefighting, flotation of minerals, and waste water treatment [1–7]. In contrast to these applications, stable foams are undesirable and need to be controlled in situations such as lubrication, textile dyeing, fermentation, and pulp and paper production [8–11]. Emulsions are equally common and find important applications in food manufacturing processes, personal and health care product development, enhanced oil recovery, paints, pharmacy, and road construction [12–15]. In contrast to these applications, stable emulsions are undesirable and have to be controlled during lubrication, desalting of crude oil, and fractionation of petroleum products [16–19].

Motivated by the need to control the stability of foams and emulsions for different applications, researchers have developed a wide variety of experimental platforms to study the stability of these colloidal systems. Broadly, the existing experimental platforms can be classified as bulk foam/emulsion setups, single film setups and single bubble/drop setups.

Bulk foam and emulsion experiments probe the physics of these colloidal systems at a bulk scale. They best mimic real life foams and emulsions, and capture all their complexity including many body interactions, the effects of advection, and the presence of plateau borders. Other advantages include the ease of operation and the convenient measurement of the aggregate properties. Common bulk foam tests include the industry standard ASTM D892 [20], the foam rise test [21], the shake test [21], and the Flender foam test [22]. Common bulk emulsion tests include the industry standard ASTM D1401 [23] and the shake test [24]. Less common bulk emulsion tests include high pressure homogenization (microfluidization) [12, 25] and membrane emulsification tests [26, 27]. Detailed reviews on bulk foam and emulsion experiments and the corresponding characterization techniques are available in the literature [21, 26, 28–33]. Despite their advantages, these tests are not suitable to systematically probe stabilization mechanisms due to the shear complexity of bulk foams and emulsions. Simplifications like 2D foams do exist [34], however, these systems are still inconvenient for developing a detailed understanding of the stability of thin liquid films that ultimately sustain foams and emulsions. To overcome the limitations of bulk tests, researchers have developed a couple of other techniques.

Email addresses: vinny@stanford.com (V. Chandran Suja), ggf@stanford.com (G.G. Fuller)

Single film techniques - the simplest abstraction of foams and emulsions - probe the stability of films that are analogous to those formed when two particles of the dispersed phase (gas bubbles or liquid drops) come close to each other [35]. Perhaps the most well known single film setup is the Scheludko-Exerowa cell, which was originally developed by Derjaguin and subsequently improved by Scheludko, Exerowa and Mysels [32, 36–38]. Other variants include the Exerowa-Scheludko porous plate cell, the Mysels cell and the Dippanear cell [3, 39–41]. Single film experiments have transformed our understanding of thin film stability. In particular, due to the ability of the technique to measure the pressure in the film, usually through a Scheludko-Exerowa cell, a deep understanding of the role of disjoining pressure in terminal thin film drainage and thin film stability has been developed [42]. Further, single film results have also aided in improving the theoretical understanding of thin film drainage, as the inherent reflection symmetry [35] in these experiments have made them attractive for theoretical and numerical analyses [43]. Detailed reviews on single film setups and results are available in the literature [32, 44]. Despite the above advantages, single film experiments have certain limitations including difficulties in conveniently controlling the size of the film and the approach velocity of the interacting interfaces, and the inability to study the interaction of interfaces with different radii of curvature.

To address these limitations and complement single film experiments, researchers have developed a third class of experimental tools that, in terms of mimicking real life foams and emulsions, fall midway between bulk tests and single film tests. These are referred to as single bubble/drop setups and, as their name indicates, utilize complete bubbles and drops to respectively understand foam and emulsion stability [45]. Single bubble/drop experiments have three notable advantages over single film tests. Firstly, single bubble/drop experiments allow the use of a complete bubble/drop, thus enabling the effects of the dispersed phase size and the rise velocity [1] to be independently studied. Secondly, single bubble/drop experiments can probe the interaction of interfaces with different radii of curvature, and have notably improved the understanding of coalescence at flat liquid-air interfaces [8, 9, 46]. Thirdly, in situ interfacial rheology measurements can be conveniently performed in single bubble/drop setups, thus making them a more holistic tool for developing a mechanistic understanding of thin film stability [46, 47].

In this manuscript, we provide a comprehensive review of this important technique along with the recent developments in foam and emulsion science that came about through single bubble/drop experiments. We start with a brief discussion of the history of single bubble/drop experiments in ***Section 2***. Subsequently, in ***Section 3*** we

describe the single bubble and single drop setups in detail. The relevant experimental protocols and data analysis techniques include (a) the construction of cumulative coalescence time distributions for ranking foam and emulsion stability, (b) the measurement of the spatiotemporal thin film thickness for understanding film thinning dynamics and predicting foam/emulsion density, and (c) the measurement of various interfacial rheological properties for mechanistically understanding the relevant foam/emulsion stabilization mechanisms. In ***Section 4*** and ***Section 5*** we present the recent developments in foam and emulsion science, respectively. Finally, we conclude the manuscript by presenting important venues for future research.

2. Historical Perspective

In this section we will provide a brief overview of the important historical developments in the field of single bubble and single drop experiments. Comprehensive historical details on single film can be found in Gochev et al. [48].

The early scientific interest in soap bubbles can be traced back to experiments performed by Boyle and Hooke [49]. Initial scientific attention was focused on understanding the origin of the colors on soap bubbles. Notably, Newton performed experiments showing that the first bright color corresponds to a thickness of 107 *nm* [48] - a remarkably accurate result (see Fig.4). Subsequently, pioneered by the efforts of Plateau, the attention shifted to understanding the shape, interfacial properties, and stability of soap films.

Investigations into the shape of soap films had a profound impact in the fields of differential geometry, calculus, and mechanics. Notably, the field of *Calculus of Variations* came about in part due to efforts by Bernoulli and his student Euler in the early 1700's to understand minimal surfaces formed by soap films [50]. The research into the shape of soap bubbles also resulted in the development of the famed Young-Laplace equation, the consequences of which were demonstrated elegantly by Charles Vernon Boys in a number experiments to the public [51]. These advancements also paved the way for the development of the Axisymmetric Drop Shape Analysis (ADSA) and the Maximum Bubble Pressure Method (MBPM), two of the common techniques used to measure the surface tension using a bubble/drop supported on a capillary. ADSA was developed as a result of efforts since the late 1800's, notably by Worthington [52, 53], to utilize the shape of pendant liquid drops as the means to measure the interfacial tension. Over the years, as a result of advances in imaging and in computational methods, ADSA has become an indispensable tool for measuring interfacial tension [54]. The first documented work on MBPM was reported by Simon in 1951 [55]. Over the years as result of the efforts of number of researchers, MPBM is one of the most popular techniques to measure dynamic surface tension [56]. Interestingly, the famed quantum mechanist Erwin Schrodinger in 1915 provided the first accurate correction for MBPM measurements where the effects of gravity cannot be neglected [57], before developing the other equation he is now known for.

Detailed investigations into the interfacial rheological properties were also spawned in part as a result of Plateau's studies, where he claimed (though incorrectly in that setting [58]) the existence of an interfacial viscosity through his description of the damping of a needle oscillating on the surface of an aqueous surfactant solution [59]. Interestingly, it was single drop experiment results – the Stokes motion of liquid droplets – that led Boussinesq to formulate the first mathematical description of interfacial viscoelasticity in 1913 [58, 60]. These results were later generalized for a Newtonian interface by Scriven in 1959 [61]. In the subsequent years, techniques employing the controlled dynamic deformation of bubbles and drops were developed as a means to measure interfacial properties. Notably, efforts by Lunkenheimer and others in 1970's formed the basis for oscillating bubble/drop rheometers [62], while efforts by Darsh Wasan and others formed the basis for expanding and contracting bubble/drop rheometers [63].

The stability of single bubbles and drops has attracted the attention of researchers since the 1800's due its fundamental [64] and practical importance [35, 65]. Some of the initial single bubble/drop experiments, notably by Lord Rayleigh [64] and Geoffrey Ingram Taylor [66], probed the bubble/drop stability against breakup in electrical fields. Single bubble experiments, notably by James Dewar, were also commonly used to study the important phenomenon of diffusion across liquid interfaces [67]. One the earliest reported schematics that we can now identify as a single bubble/drop setup for studying bubble/drop stability can be observed in Fig. 54 of Charles Vernon Boys' popular book *Soap-Bubbles and the forces which mould them* [51]. Early investigations into thin film stability by Derjaguin and Kussakov that predated the development of the famed DLVO theory were also performed with single drop experiments [68]. More practical versions of single bubble/drop setups can be seen in the works of Rehbinder and Wenstrom [69], while a feature complete version of a single bubble setup consisting of an arrangement to form bubbles in a controlled way along with an interferometry setup for measuring the film thickness can be found in a work published by Stanley Mason in 1960 [70].

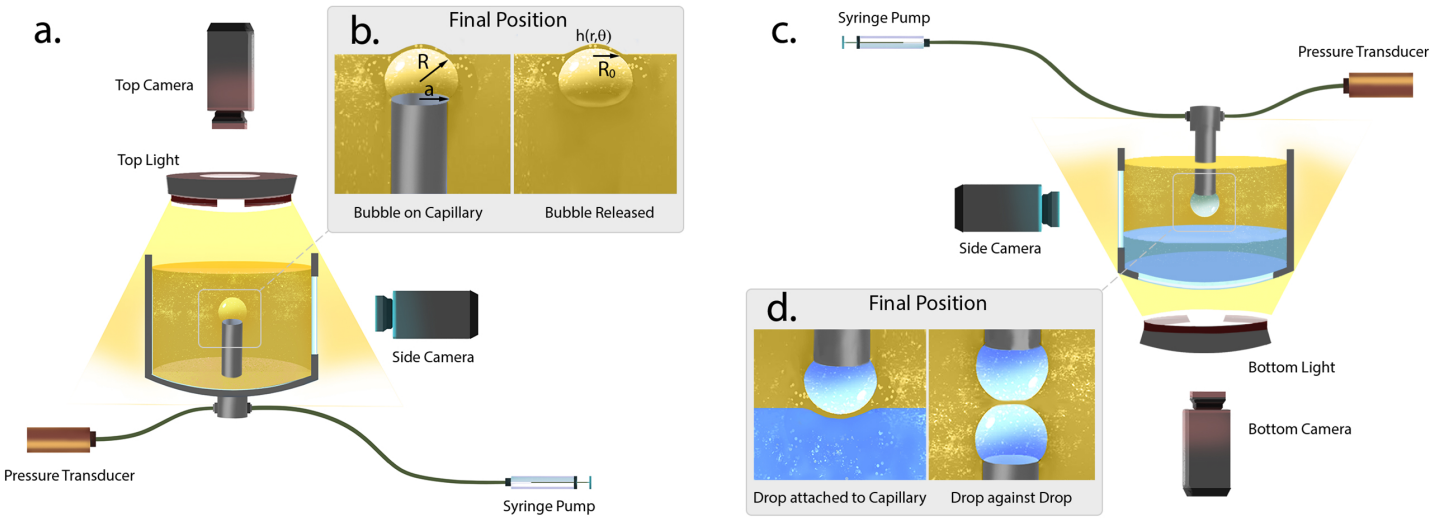

Figure 1: Schematic of single bubble and drop setups. (**a.**) A schematic of a single bubble setup with the labeled components. (**b.**) The final positions of the bubble for different variations of the setup. These include the cases where the bubble is attached to the capillary (left) and when it is released from the capillary (right). Here, R is the radius of curvature of the undeformed bubble, $h(r, \theta)$ is the film thickness as a function of the radial position r and angular position θ, and R_0 is the radial extent of the film visible during thin film interferometry measurements. (**c.**) A schematic of a single drop setup with the labeled components. Here, the drop is denser than the ambient liquid. (**d.**) The final positions of the drop for different variations of the setup. These include the cases where the drop is attached to the capillary (left) and when interactions occur between two drops attached to capillaries (right).

3. Methods

3.1. Single bubble and single drop setups

Single bubble and single drop setups provide a convenient framework to study in detail the dynamics of bubble-bubble and drop-drop interactions. Such an understanding is crucial to predict and tune the various aspects of foams and emulsions, including their stability [8] and density [71].

A typical schematic of a single bubble and single drop setup is shown in Fig. 1. A single bubble setup (Fig.1.a) commonly consists of a chamber to contain the ambient liquid, a capillary, and a syringe pump to form the bubble. In many cases, a pressure transducer is also connected to the capillary for monitoring the bubble pressure. The bubble pressure data is useful for many purposes including determining coalescence events (see ***Section 3.2***) and measuring the rheological response of the air-liquid interface (see ***Section 3.4***). The profile of the bubble is visualized by a side camera, while the spatiotemporal evolution of the ambient liquid between the bubble and the air-liquid interface is visualized by the top camera (see ***Section 3.3***). Further details of the setup depend on the type of the single bubble experiment.

The different types of single bubble experiments reported in literature can be broadly classified into three categories. Namely, bubble attached to a capillary interacting with a flat air-liquid interface [8, 9, 46, 47, 71–74], bubble released from a capillary interacting with an air-liquid interface [75–81], and bubble attached to a capillary interacting with another bubble on a capillary [82]. The final position of the bubble for two of these variants is shown in Fig.1b. Each of the above single bubble variants has specific advantages. The first variant, where the bubble remains attached to the capillary, is very well suited for studying thin film dynamics using interferometry, as the bubble position can be accurately controlled. Further advantages include the ability to easily control the ascend velocity and the size of the bubble. The second variant, where the bubble is released from the capillary, offers a convenient framework to study the bounce dynamics [77, 78, 80] of a freely rising bubble at an air-liquid interface. Finally, the third variant with two bubbles is very well suited to study bubble-bubble coalescence. These experiments are also more amenable to mathematical modelling due to the additional reflection symmetry in the physical configuration. The specific protocols corresponding to experiments in these different categories are described in the above references and are discussed to some extent in ***Section 4***. For illustration, we outline below a protocol commonly followed for experiments in the first category.

At the start of a single bubble experiment where the bubble remains attached to the capillary, fluctuations in the size of the bubble can be detected by monitoring the pressure inside the bubble. After establishing the size stability of

the bubble, the experiment starts by moving the bubble at a fixed velocity towards the air-liquid interface from its initial to its predetermined final position (Fig.1b). In practice, for keeping the bubble in focus for interferometry measurements, the positioning of the bubble is accomplished by lowering the air-liquid interface towards the bubble by mechanically moving the chamber downwards. The final position of the bubble is usually selected such that it corresponds to the equilibrium position attained by a free bubble through the balance of buoyancy and capillary forces. The top camera records the spatiotemporal evolution of the film of liquid between the bubble and the air-liquid interface. As the film drains and its thickness becomes comparable to the wavelength of light, interference patterns are seen by the top camera (eg. see Fig.4). Finally, the experiment ends as the film ruptures and the bubble coalesces at some critical film thickness. The coalescence time is accurately identified with the help of a pressure transducer. The details on analyzing the coalescence times and interference patterns are provided in the subsequent subsections.

Single drop setups are broadly similar to single bubble setups. Since drops can either be lighter or heavier than the ambient liquid, single drop setups often have the capability to orient and move the drop in the direction of its natural motion (Fig.1c). As with the single bubble setup, there are three common variants of single bubble setups reported in the literature. Namely, drop attached to a capillary interacting with a flat liquid-liquid/solid interface [17, 83], drop released from a capillary interacting with a liquid-liquid/gas interface [76, 84–89], and drop attached to a capillary interacting with another drop on a capillary [1, 82, 90, 91]. The final drop position for two of these variants is shown in Fig.1d. The protocols and advantages of the single drop variants more or less mirror those of single bubble setups and are discussed in context in ***Section 5***.

3.2. Coalescence time distributions

A major observable from single bubble/drop experiments is the time it takes for a bubble or a drop to coalesce against a suitable air/liquid-liquid interface. This quantity is commonly referred to as the coalescence time. The coalescence time of single bubbles and drops is physically correlated to the stability of foams [8, 9] and emulsions [24], respectively, and provides a convenient way to predict and rank foam and emulsion stability. Unfortunately, directly using coalescence times to assess foam or emulsion stability might not give the intended results due to following three reasons. Firstly, single bubble/drop coalescence times are inherently stochastic [8, 92, 93]. Secondly, the presence of coalescence modifiers such as antifoams or demulsifiers can lead to very large variations in the measured coalescence times [9]. Thirdly, coalescence times may have temporal trends [46, 94]. Hence, rigorously predicting and ranking foam and emulsion stability from single bubble/drop measurements, requires careful statistical analysis. One such possibility is the use of coalescence time distributions.

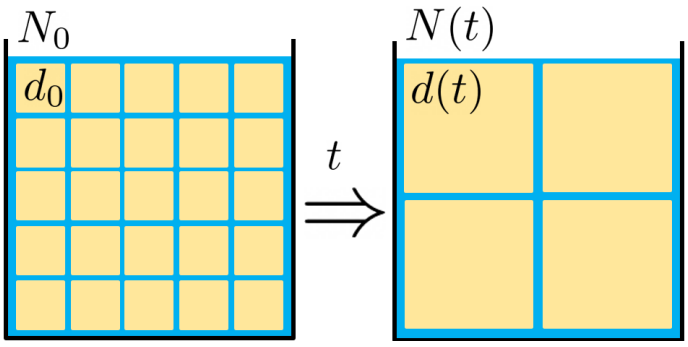

Figure 2: Schematic of an emulsion as a stack of mono-disperse cubic cells that decease in number and increase in size as time passes.

To understand the fundamental concept of coalescence time distributions and its relation to foam/emulsion life time, let us analyze single bubble/drop experiments from a more analytical point of view. For illustrative purposes we will use a simple emulsion model [95, 96]. Consider an emulsion as a stack of N_0 mono-disperse cubic cells of size d_0 (Fig. 2). Without changing the volume of the continuous and disperse phases, let's assume that coalescence events take place in such a way that, as time passes, the emulsion becomes a stack of $N(t) < N_0$ mono-disperse cells of size $d(t) > d_0$. As coalescence is a random process, it is reasonable to assume that the lifetime of a specific thin film separating two cells, τ_{tf}, should be inversely proportional to the area of the thin film (A) and the probability of coalescence per unit area and time (f), i.e.

$$\tau_{tf} \approx \frac{1}{Af}, \tag{1}$$

From Eq. 1, the number of cells must verify

$$\frac{dN(t)}{dt} = -fA_t(t), \tag{2}$$

where $A_t(t)$ is the total surface area. Since we are considering a cubic cell system, Eq. 2 can be rewritten as

$$\frac{dN(t)}{dt} = -3fN(t)d^2(t). \tag{3}$$

As above-mentioned, the volume of the disperse phase is constant, so that

$$N(t)d^3(t) = k, \tag{4}$$

being k a constant. Combining Eqs. 3 and 4 and integrating with respect time, we obtain the following relation (see ***Appendix B*** for details),

$$\frac{1}{d_0^2} - \frac{1}{d^2(t)} = 2ft. \tag{5}$$

In spite of the simplicity of this model, the linear relation between $1/d^2(t)$ and t has been experimentally observed [96]. The foam/emulsion lifetime, τ, can be obtained from Eq. 5 by imposing $1/d^2(\tau) = 0$ as,

$$\tau = \frac{1}{2d_0^2 f}. \tag{6}$$

As explained in ***Section 1***, bulk foam/emulsion experiments have a high degree of complexity due to many body interactions, effects of advection, and the presence of plateau borders. Single bubble/drop experiments simplify the experimental approach to the problem by allowing for the systematic measurement of quantities such as the critical film thickness, drainage rates and the interaction forces. In addition, the measurement of bulk emulsion/foam stability is also feasible, since a convenient number of single bubble/drop experiments allows one to construct a coalescence time distribution (Fig.3). This statistical distribution characterizes the frequency of coalescence events f previously described and is therefore directly related to the emulsion/foam lifetime as shown in Eq.6.

An early use of coalescence time distributions can be seen in a work by Stanley Mason and co-workers, where they used a Gaussian distribution to capture the stability of surfactant-laden bubbles [70]. Since then, a number of statistical distributions including the Weibull [97], Rayleigh [8, 9, 92], and custom distributions [94, 98, 99] have been used to capture life time of bubbles [8, 9, 92, 94, 97–99], drops [24, 100], and antibubbles [93]. Despite the variety of distributions reported in the literature, interestingly, most of the commonly used coalescence time distribution can be shown to be a form of the Weibull distribution.

The Weibull distribution is a two parameter continuous distribution of positive random variables that is commonly used to describe the failure time of physical entities [101]. The distribution has the following cumulative distribution function,

$$P_w(t;\lambda;k) = 1 - e^{-(t/\lambda)^k}. \tag{7}$$

Here t, λ, k are positive quantities, with t denoting the measured coalescence time, λ dictating the scale of the distribution, and k dictating the shape of the distribution. The values for λ and k are usually obtained from their maximum likelihood estimators (see ***Appendix C***). Two of the other commonly used distributions, the Rayleigh distribution and the distribution reported by Villermaux and coworkers (hereon the Villermaux distribution) are variants of Weibull distribution with different values for λ and k.

The Rayleigh distribution is obtained by setting $\lambda = \sqrt{2}\sigma$ and $k = 2$. The corresponding cumulative distribution function becomes,

$$P_r(t;\sigma) = 1 - e^{-t^2/(2\sigma^2)}. \tag{8}$$

Here, σ is the scale parameter of the distribution and is usually obtained from the maximum likelihood estimation method (see ***Appendix C***).

The Villermaux distribution is obtained by setting $\lambda = \tau_0$ and $k = 4/3$. The corresponding cumulative distribution function becomes,

$$P_v(t;\sigma) = 1 - e^{-(t/\tau_0)^{4/3}}. \tag{9}$$

Here, τ_0 is the scale parameter of the distribution and is obtained from physical considerations as

$$\tau_0 = \left(\frac{4}{3\epsilon}\right)^{3/4} \left(\frac{R}{l_c}\right)^{1/2} \frac{\mu l_c}{\sigma_{\alpha\beta}}, \tag{10}$$

where R is the radius of the bubble, l_c is the capillary length, μ is the dynamic viscosity of the ambient fluid, $\sigma_{\alpha\beta}$ is the surface tension, and ϵ is an *ad hoc* parameter that characterizes the bubble rupture efficiency.

In figure 3, we compare the above three probability distributions in describing the distribution of coalescence times measured in four different systems - bubbles in deionized water [94], antibubbles in a 10% mixture of glycerol in water [93], silicone oil drops in an aqueous polymer mixture [24], and bubbles in lubricants with antifoam [9]. The scale and shape (when applicable) were obtained from the maximum likelihood estimators, while the mixture ratios (when applicable) were obtained using the expectation-maximization algorithm (see ***Appendix C***). The Kolmogrov-Smirnov (KS) p values of the obtained distributions are indicated in the figure legend, while the parameters and R^2 values of the distributions are available in ***Appendix C***. It is worth noting that the obtained shape parameter is greater than 1 in all the cases, which in the context of Weibull distribution physically implies that coalescence is more likely to happen as time proceeds.

As expected, we observe that the generic two parameter Weibull distribution best describes all the experimental data. This observation is supported by the high values of the KS p metric. Despite the high fit fidelity, the presence of two parameters leads to practical difficulties such as ranking the coalescence stability and using the expectation-maximization algorithm [102] for robustly determining the

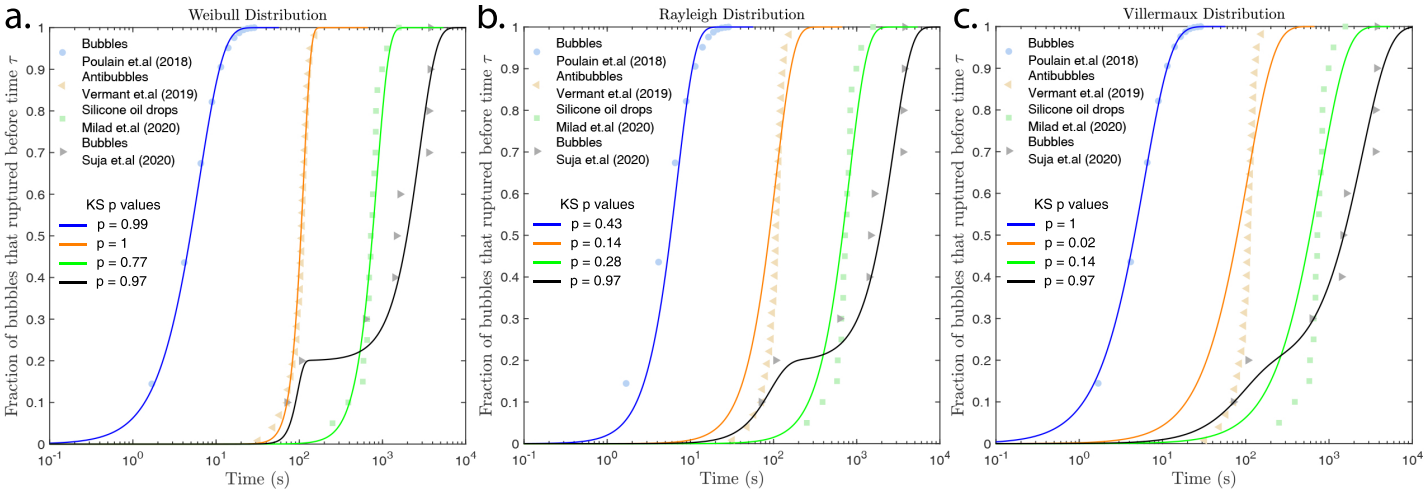

Figure 3: Comparison of three different probability distributions in capturing the distribution of coalescence times measured in four different systems: ● Bubbles in deionized water [94], ◀ Antibubbles in a 10% mixture of glycerol in water [93], ■ Silicone oil drops in an aqueous polymer mixture [24], and ▶ Bubbles in lubricants with antifoam [9]. The Kolmogrov-Smirnov (KS) p values are indicated in the legend. (**a.**) The two parameter Weibull distribution fit to the experimental data using the Maximum Likelihood Estimaters (MLE) of the scale and shape parameter. (**b.**) The one parameter Rayleigh distribution fit to the experimental data using the MLE of the scale parameter. (**c.**) The one parameter Villermaux distribution fit to the experimental data using the MLE of the scale parameter. The parameters and R^2 values of the plotted distributions are available in ***Appendix C***.

different distributions in the experimental data (see ***Appendix C***). The one parameter Rayleigh distribution is observed to broadly describe all the tested experiments. This observation is supported by the moderate values of the KS p and R^2 metrics. Despite having only empirical evidence for its suitability [8, 9, 92], the Rayleigh distribution is a very convenient method for ranking the coalescence stability of diverse systems and for robustly representing the mixture distributions in the experimental data. The one parameter (ϵ in Eq.10 is a free parameter) Villermaux distribution is observed to very accurately describe the coalescence time distributions involving bubbles, while it appears to be relatively inaccurate when it comes to antibubbles and drops. This observation is supported by the high values of the KS p and R^2 metrics for bubbles and relatively low values of the same metrics for the other systems. This is not surprising as the Villermaux distribution was derived for bubbles based on physical considerations [99], and is a very convenient choice for describing bubble lifetimes and ranking bubble stability. It would be interesting for future studies to develop distributions utilizing physical arguments that can capture the experimental trends in antibubbles and drops. Particularly, these new distributions should be able to physically account for the variance in the measured coalescence times that appears to scale inversely with the dispersed phase viscosity.

3.3. Thin film profile reconstruction

Measuring the spatiotemporal evolution of the film thickness is crucial for obtaining mechanistic insights into foam and emulsion stability. This information is also useful for predicting foam and emulsion density. The film thickness data can be readily obtained from single bubble/drop experiments through the integration of a thin film interferometry apparatus.

Commercial and custom made interferometry apparatuses have been widely used in the literature for thin film thickness measurements. Commercial interferometers reported in the literature include those produced by Filmetrics [103, 104], Zygo [105, 106], and Horiba [107], among others. These interferometers are particularly efficient at high frequency automated thickness measurements at low spatial resolutions, often restricted to a single point. In many scenarios involving foam and emulsion films, it is necessary to measure the film thickness at both high temporal and spatial resolutions. This has motivated a number of researchers to perform studies with custom built thin film interferometry apparatuses [8, 9, 17, 43, 46, 47, 71, 75, 83, 85, 108–122].

As shown in Fig.1, these custom built interferometers generally consists of a light source, an optical train, and a photo-detector. Common light sources include laser based monochromatic [112, 113, 115, 116], optically filtered LED based monochromatic [83], and LED or halogen based broadband sources [8, 9, 17, 46, 47, 71, 117–119, 123]. Com-

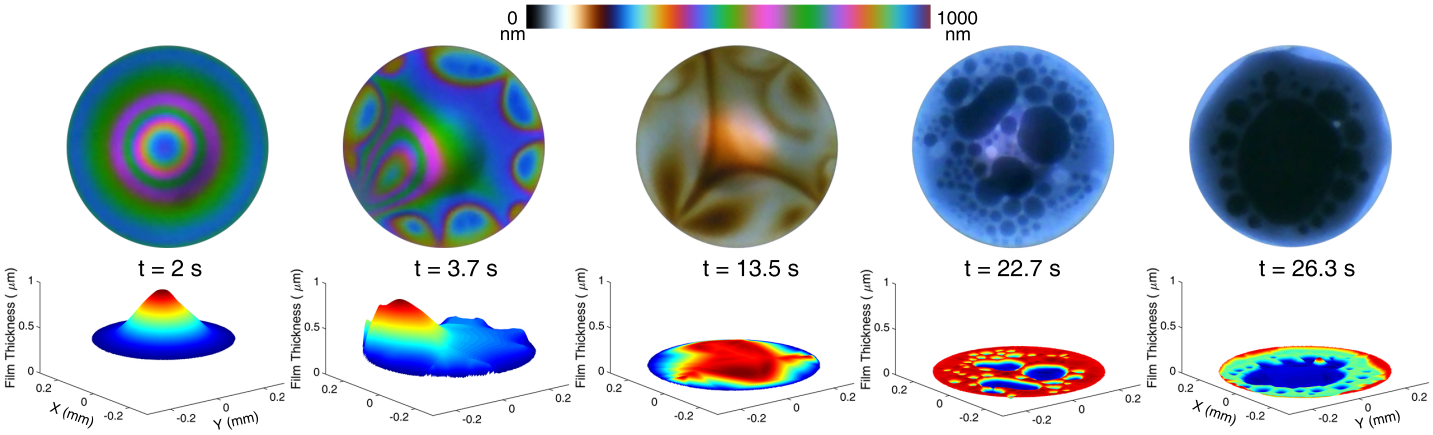

Figure 4: A sequence of interferograms observed over a bubble in a 10 mM CTAB solution and the corresponding physical film thickness profiles reconstructed utilizing Eq.D.1 (see Appendix D). The corresponding time stamps are indicated below the interferograms with $t = 0$ indicating the time at which the bubble encounters the flat air-water interface. The theoretical color map used for the reconstruction of the film profiles is shown at the top. Note that in the reconstructed film profiles, the blue and red colors correspond respectively to the minimum and maximum film thickness for each plot, and that the absolute film thickness can be inferred from the relative position of film profile about the z axis.

mon optical components include a lens assembly usually in the form of microscope objectives [83, 112, 115] or telecentric lenses [8, 46, 71, 118], and optical filters [71, 83, 85, 123]. Routinely used photo-detectors to image the interferograms include cine [85], CCD [123], and CMOS [71, 116] cameras. The obtained interferograms are then decoded to obtain the underlying film thickness. This is accomplished by utilizing results from the theory of thin film interference.

Two common formulations are commonly used in literature to relate interferograms to film thicknesses. The first formulations considers the first two reflections and neglects contributions from higher order reflections on the obtained interferogram, resulting in the following relation,

[123, 124],

$$\frac{I(\lambda,h)}{I_0(\lambda)} = \Re_1 + \Re_2(1-\Re_1)^2 + 2\sqrt{\Re_1\Re_2(1-\Re_1)^2}\cos(\phi)\,, \tag{11}$$

$$\phi = \frac{4\pi n_2 h}{\lambda} + \pi(\mathbb{1}(n_2 > n_1)) + \pi(\mathbb{1}(n_3 > n_2)). \tag{12}$$

Here, h is the film thickness, n_x is the refractive index, ϕ is the phase difference between the interfering reflected beams and $\mathbb{1}$ is the indicator function that captures the phase shift of π radians that occurs when light reflects off a medium with a higher refractive index. $\Re_1$ and $\Re_2$ are the power (intensity) reflectivity coefficients obtained from the Fresnel equations (see ***Appendix D*** for details).

In the second formulation, considering all the reflected waves, we can obtain the following expression between the film thickness and light intensity in the interferogram [38, 125],

$$h = \frac{\lambda}{2\pi n_2}\left(l\pi \pm \arcsin\sqrt{\frac{\Delta(1-r_{23}r_{21})^2}{(1-r_{23}r_{21})^2 + 4r_{23}r_{21}(1-\Delta)}}\right). \tag{13}$$

Here, $\beta = 2\pi n_2 h/\lambda$, l is a whole number that denotes the order of interference and r_{xy} are the amplitude reflectivity coefficients obtained from the Fresnel equations (see ***Appendix D*** for details). The common protocols for determining l as well as the details related to using Eq. 13 to recover film thickness profiles are available in the literature [81, 108, 112, 125].

Eq.13 is a convenient choice when experiments are performed using monochromatic light sources in situations where the order of interference (l) can be easily inferred. On the other hand, when broadband light sources are used or when it is difficult to determine l (eg. for films that do not thin below a few hundred nanometers), Eq.D.1 is a convenient choice. Note that the truncation error in using Eq.D.1 is $\mathcal{O}(r_{xy}^8)$, which in almost all practical cases is negligible (see ***Appendix D***).

We will conclude this section by touching upon techniques apart from traditional interferometry that have been used to measure the spatiotemporal profiles of thin liquid films. Planar laser induced fluorescence (PLIF) is a common technique used to visualize liquid films [89, 126, 127], and is particularly well suited to study thick (sub-millimeter scale) films. Hyperspectral interferometry is a technique in development that has improved robustness against imaging noise [128]. Digitally holography is a promising technique that has recently been employed visualize bubbles [129].

The large measurement range and high spatiotemporal resolution of digital holography could make this the technique of choice for future studies involving thin films.

3.4. Interfacial rheological properties

The stability of foams and emulsions is significantly influenced by the rheological properties at the fluid-fluid interface [1, 46, 47, 58, 130–138]. These so-called "complex" or "non-Newtonian" interfaces arise due to the presence of adsorbed surface active species, which can laterally interact and form microscopic networks that allow the interface to support both shear and normal stresses [58, 61, 104, 139]. Unlike simple interfaces, these stresses can occur in the absence of a finite curvature or gradients in surface tension [58].

Complex interfaces exhibit a viscoelastic response to surface deformations. In other words, the resulting stress exhibits both a strain-dependent (elastic) and a strain rate-dependent (viscous) response [54, 58, 134, 139–141]. Non-Newtonian interfaces are thus described via rheological constitutive equations that take into account the time-, position-, and velocity-dependent nature of their viscoelastic properties [54, 58, 134, 139–141].

For a general viscoelastic liquid interface, total interfacial stress tensor $\boldsymbol{\sigma}$ can be expressed as [104, 135],

$$\boldsymbol{\sigma} = \sigma_{\alpha\beta}(\Gamma)\boldsymbol{I}_s + \boldsymbol{\sigma}_e. \tag{14}$$

Here, $\sigma_{\alpha\beta}(\Gamma)$ is the static equilibrium value of the interfacial tension between phases α and β as a function of surface species concentration (Γ) and $\boldsymbol{I}_s$ is the second order surface identity tensor. The interfacial tension is a scalar thermodynamic quantity that provides a measure of the work required to increase the surface area of an interface [142, 143]. $\boldsymbol{\sigma}_e$ is the extra rheological stress arising from viscous and elastic deformations. This stress is represented as a rank-2 tensor that describes how in-plane stresses propagate along each of the interfacial coordinate directions. In its most general form, this tensor is non-isotropic [133, 134, 141]. The remainder of this article will focus on displacements and stresses that exist purely in the tangential direction; for a discussion on bending and normal stresses, the reader is directed to references [144–149].

A general viscoelastic interface will have both a viscous and an elastic contribution to the extra stress, thus requiring an appropriate viscoelastic model to capture the combined contribution of viscous and elastic deformations. Depending on the nature of the interface and the deformation, a number of relations are available in the literature for calculating the extra rheological stresses. For example, for a purely viscous Newtonian interface, $\boldsymbol{\sigma}_e$ can be obtained from the Boussinesq-Scriven equation as [61, 150]

$$\boldsymbol{\sigma}_e = \left[(k_s - \eta_s)\,\nabla_s \cdot \boldsymbol{v}_s\right]\boldsymbol{I}_s + 2\eta_s \mathbb{D}_{\boldsymbol{s}}, \tag{15}$$

where ∇_s is the surface gradient operator, $\boldsymbol{v}_s$ is the surface velocity vector, and $\mathbb{D}_{\boldsymbol{s}}$ is the surface rate of deformation tensor, equal to $\frac{1}{2}\left(\nabla_s \boldsymbol{v}_s + (\nabla_s \boldsymbol{v}_s)^T\right)$. Eq. 15 shows that $\boldsymbol{\sigma}_e$ depends on two material properties, namely the surface dilatational viscosity (k_s) and the surface shear viscosity (η_s). Much like their bulk fluid counterparts, complex interfaces can support stresses when subject to shearing deformations and are similarly characterized by a shear viscosity [58, 61]. However, unlike bulk liquids, which behave as incompressible fluids in normal operating conditions, fluid-fluid interfaces are able to change their surface area when subject to dilatational or compressional deformations, and subsequently are also characterized by an interfacial dilatational viscosity [58, 61].

For a purely elastic interface undergoing small deformations, $\boldsymbol{\sigma}_e$ can be obtained from infinitesimal strain theory as follows [135]

$$,\boldsymbol{\sigma}_e = \left[(K_s - G_s)\,\nabla_s \cdot \boldsymbol{u}_s\right]\boldsymbol{I}_s + 2G_s \mathbb{U}_{\boldsymbol{s}}, \tag{16}$$

where $\boldsymbol{u}_s$ is the surface displacement vector and $\mathbb{U}_{\boldsymbol{s}}$ is the surface deformation tensor, equal to $\frac{1}{2}\left(\nabla_s \boldsymbol{u}_s + (\nabla_s \boldsymbol{u}_s)^T\right)$. Analogous to the viscous contribution, $\boldsymbol{\sigma}_e$ is a function of the surface dilatational modulus (K_s) and the surface shear modulus (G_s). Alternatively, for larger deformations, the Neo-Hookean model for an elastic interface can be used [135, 151].

In this section, we will discuss how single bubble/drop setups can also be used as a convenient platform with little modification to measure the static and dynamic interfacial stress, and the surface dilatational properties. The measurement of these interfacial properties is necessary for predicting the drainage dynamics [47, 71], the rupture dynamics [152] and overall stability of foams and emulsions [137, 138].

3.4.1. Static and Dynamic Interfacial Stress

Pendant drop tensiometry

Pendant drop tensiometry is a common and robust technique for measuring the interfacial stress of liquid-liquid and liquid-air interfaces [54, 153]. In this method a pendant drop is formed on a capillary and its shape is iteratively fit to the theoretical shape obtained from the interfacial stress balance [54, 153].

For simple interfaces, the static and dynamic interfacial stress is solely determined by the interfacial tension, $\sigma_{\alpha\beta}(\Gamma)$, which is constant and isotropic along the drop's

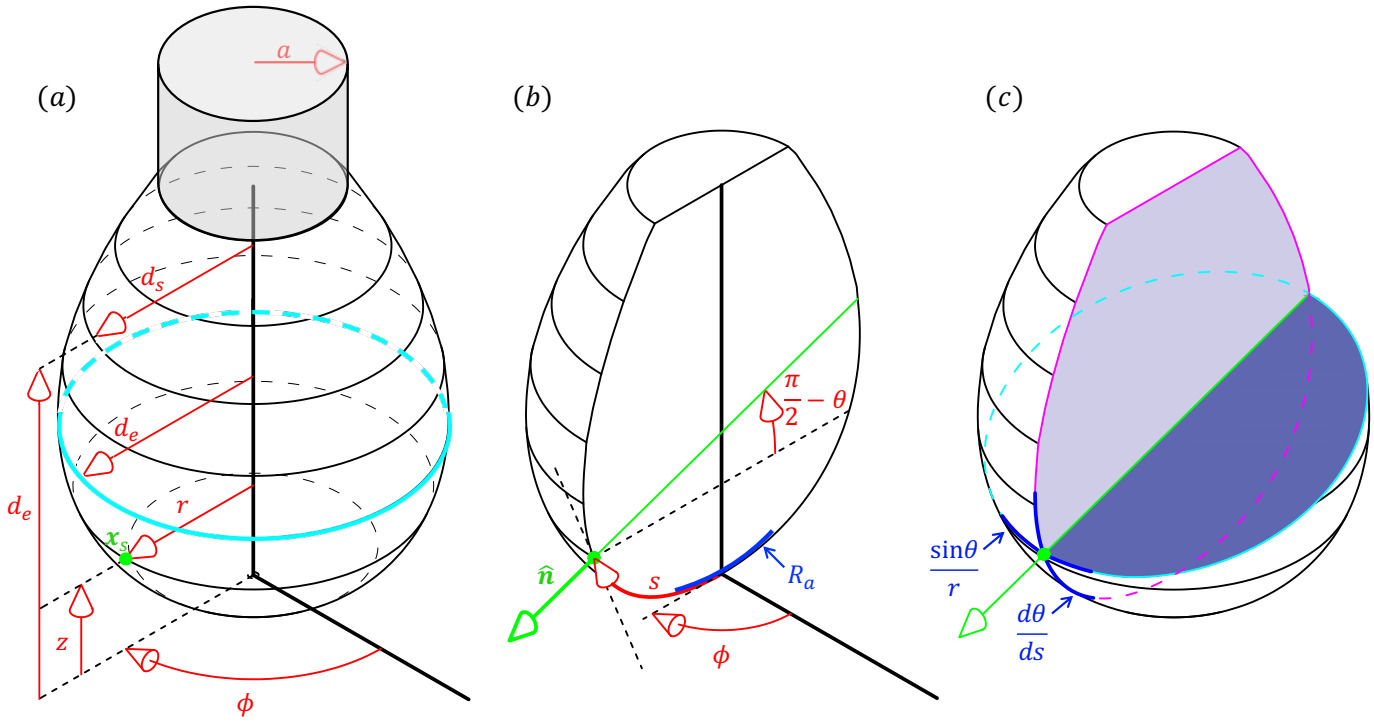

Figure 5: Schematic of an axisymmetric pendant drop suspended from a capillary with radius a. (**a.**) A point on the surface of the drop, $\boldsymbol{x}_s$, can be uniquely described using a cylindrical coordinate system $(r - z - \phi)$. d_s and d_e denote diameters (only half extend is shown) used in the method of the selected plane to calculate $\sigma_{\alpha\beta}$. (**b.**) The coordinate system is projected onto the $s - \phi$ frame, where s is the arc length measured from $z = 0$ and ϕ is the azimuthal angle. θ is the angle formed between s and the horizontal plane, such that $\pi/2 - \theta$ is the angle between the horizontal plane and the surface unit normal $\hat{\boldsymbol{n}}$. R_a is the radius of curvature at the drop apex. (**c.**) The principal curvatures $\frac{d\theta}{ds}$ and $\frac{\sin\theta}{r}$ are locally tangent to the s- and ϕ-coordinates, respectively.

surface [58, 142, 143, 154]. A convenient way to measure $\sigma_{\alpha\beta}(\Gamma)$ is through the so called Axisymmetric Drop Shape Analysis (ADSA) method, whereby the interfacial tension is obtained by analyzing the shape of a stationary pendant drop in a gravitational field [54, 134, 153]. The shape of the axisymmetric drop is set by a balance between gravitational deformation and surface tension restoration, represented by the dimensionless Bond number, $Bo = \Delta\rho g R_a^2/\sigma_{\alpha\beta}(\Gamma)$ [54, 134, 153]. Here, $\Delta\rho$ is the difference in density between the drop and the bulk, g is the gravitational acceleration, and R_a is the radius of curvature at the drop apex.

An axisymmetric pendant drop is depicted in Figure 5. Any point $\boldsymbol{x}_s$ at the surface of the drop can be described by a cylindrical coordinate system $(r - z - \phi)$ (Fig.5a). This coordinate system can be projected onto the $s - \phi$ frame, where s is equal to the arc length measured from $z = 0$ and ϕ is the azimuthal angle (Fig.5b) [134, 141]. In this coordinate system, s and ϕ are both locally tangent to $\boldsymbol{x}_s$ and are related to the cylindrical coordinates via the following transformations,

$$\frac{dr}{ds} = \cos\theta, \tag{17}$$

$$\frac{dz}{ds} = \sin\theta, \tag{18}$$

where θ is the meniscus slope angle (i.e. the angle formed between the horizontal plane and the drop interface).

This coordinate transformation allows for a facilitated determination of the drop shape and is particularly advantageous for the computation of the interfacial stress tensor for non-isotropic complex interfaces, as outlined at the end of the section [134].

Using the coordinate transformations in Eqs. 17 and 18, the isotropic value for the interfacial tension of an axisymmetric pendant drop or bubble is prescribed by the interfa-

cial normal stress balance [54, 153, 155],

$$\sigma_{\alpha\beta}(\Gamma)\left(\frac{d\theta}{ds}+\frac{\sin\theta}{r}\right)=\Delta P_a-\Delta\rho g z. \tag{19}$$

Eqs. 17 – 19 comprise a system of ordinary differential equations in curvilinear co-ordinates subject to the boundary condition,

$$r=0,\ z=0,\ \theta=0 \quad \text{at} \quad s=0. \tag{20}$$

Eq. 19 is the Young-Laplace equation, which relates the pressure jump across the interface, $\Delta P_a - \Delta\rho g z$, to the local principal meridional and parallel curvatures, $\frac{d\theta}{ds}$ and $\frac{\sin\theta}{r}$ (see Figure 5c). The pressure jump at any point along the interface can be obtained by adding the hydrostatic pressure contribution, $\Delta\rho g z$ (where $z = 0$ corresponds to the position of the drop apex), to the pressure jump at the drop's apex, ΔP_a (determined via symmetry) [54, 153]. The sign of the gravitational term depends on whether the drop is buoyant or pendant.

Eqs. 17 – 19 are iteratively solved numerically for different values of $\sigma_{\alpha\beta}(\Gamma)$ until the solution converges to the experimentally obtained drop profile [54, 153]. The accuracy of the obtained surface tension scales inversely with the square of the Worthington number, defined as $Wo = BoV_d/(2\pi a R_a^2)$, where V_d is the volume of the drop and a is the radius of the capillary [54].

Despite being the most accurate way to recover $\sigma_{\alpha\beta}(\Gamma)$ from pendant drop images, numerically solving Eqs. 17 – 19 is computationally intensive and time consuming. Alternatively, the method of the plane of inflection or the method of the selected plane may be used to determine the surface tension from pendant drop images [156]. The method of the selected plane is the more accurate method among the two, and involves recasting the bond number as $Bo_{de} = \Delta\rho g d_e^2/\sigma_{\alpha\beta}(\Gamma)$ and using the numerically tabulated values of Bo_{de} as function of the drop shape parameter $S = d_s/d_e$ to recover $\sigma_{\alpha\beta}(\Gamma)$ [156–158]. Here, d_e is the equatorial diameter of the drop and d_s is the drop diameter at a height of d_e, both which are easily obtained through image processing (Fig. 5a). Additional details of the axisymmetric drop shape analysis, including a historical perspective and a discussion of variants of the technique such as the compound pendant drop technique [159], are available in Berry et al. [54].

Although complex interfaces are described by a position-dependent interfacial stress tensor $\boldsymbol{\sigma}$, there are cases where $\boldsymbol{\sigma}$ reduces to a constant scalar value, rendering traditional shape-fitting methods valid for the interfacial energy calculation. This can be achieved in complex interfaces if the interface remains undeformed so that deviatoric viscoelastic stresses are not present. Thus, in the absence of any surface deformations, the surface stress (Eq.14) on a stress-relaxed viscoelastic interface is isotropic and constant along the drop surface, and Eqs. 17 – 20 can be used. The validity of the ADSA method for complex interfaces can be verified by plotting the local mean curvature of the surface as a function of the height along the drop; if the slope is constant, then the interfacial stress is prescribed by a constant scalar [134]. However, if a viscoelastic interface is deformed sufficiently, it will exhibit stress anisotropy. In such cases, Eq. 19 does not accurately describe the interface, and instead needs to be modified to account for the spatial and directional dependence of the surface stress.

Danov and coworkers developed a method known as Capillary Meniscus Dynamometry (CMD), whereby the components of the anisotropic interfacial stress tensor are determined for axisymmetric drops/bubbles [141]. Once again, the interfacial stress balances is simplified by projecting the coordinate system onto the $s-\phi$ frame. Since the s and ϕ coordinates are locally tangent to the principal curvatures, the interfacial stress tensor $\boldsymbol{\sigma}$ can be diagonalized and its deviatoric components expressed in terms of a pair of principal stresses as, $\boldsymbol{\sigma} = \sigma_s \hat{\boldsymbol{e}}_s\hat{\boldsymbol{e}}_s + \sigma_\phi \hat{\boldsymbol{e}}_\phi\hat{\boldsymbol{e}}_\phi$, where $\hat{\boldsymbol{e}}_s$ and $\hat{\boldsymbol{e}}_\phi$ are the unit vectors [134, 141].

In the CMD method, the interface is split into small domains and the normal and tangential stress balances are applied locally [141]

$$\sigma_s\frac{d\theta}{ds}+\sigma_\phi\frac{\sin\theta}{r}=\Delta P_a-\Delta\rho g z, \tag{21}$$

$$\sigma_\phi=\frac{d\left(r\sigma_s\right)}{dr}. \tag{22}$$

The Laplace pressure at the apex, ΔP_a, and the interface position are required as input parameters and can be determined from experimental measurements. This method was further developed by Nagel et al., who wrote a set of MATLAB routines that are available online under an open-source license [134].

Figure 6 reproduces results obtained by Danov et al. for a buoyant bubble in a 0.005 wt% aqueous solution of the protein hydrophobin HFBII [141]. The bubble was allowed to age for 320 s and the Laplace pressure at the drop apex was measured as the bubble volume was reduced in a stepwise fashion. Upon compression, the bubble shape starts to deviate from the Young-Laplace equation. The two components of the interfacial stress, σ_s and σ_ϕ, are plotted against the vertical coordinate z measured from the drop apex. Significant stress anisotropy is evidenced by the variation of σ_s and σ_ϕ along the height of the bubble. The region where σ_s adopts negative values corresponds to the appearance of wrinkles along the bubble surface.

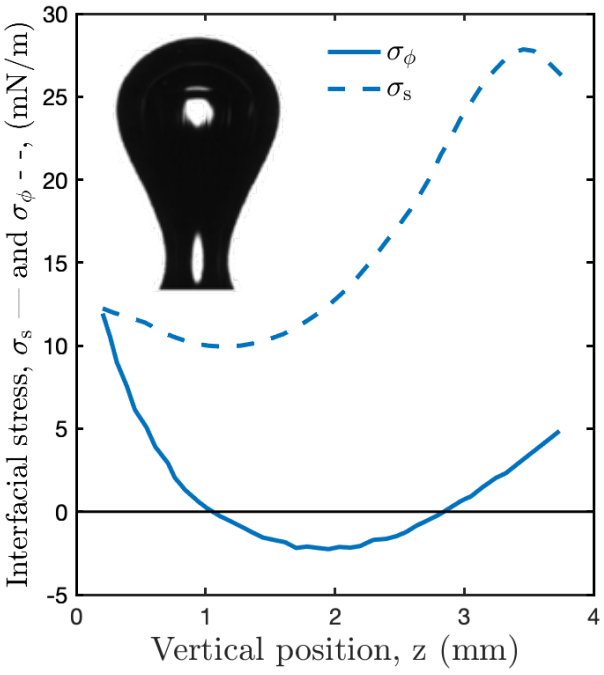

Figure 6: A buoyant bubble in a 0.005 wt% aqueous HFBII solution is allowed to age for 320 s and then compressed in a step-wise fashion. The Laplace pressure at the drop apex and the bubble shape are used to determine the anisotropic components of the surface stress, σ_s and σ_ϕ. These are plotted against the vertical coordinate z measured from the drop apex at a time of 420 s after bubble formation. Regions where σ_s adopts negative values correspond to the appearance of wrinkles along the bubble surface. Results reproduced from Danov et al. [141].

In many applications, such as for characterizing protein absorption [47] and foam generation [160], it is important to measure the dynamic value of surface stress. The axisymmetric drop shape analysis is convenient for this purpose, when the dynamic change of surface stress is slow (in the order of a few seconds) compared to time required to form a pendant drop and measure the stress. This is often the case when changes in the interfacial tension are brought about by the adsorption and rearrangement of large molecules at the interface [47, 133, 136]. On the other hand, when the change in interfacial tension is fast (on the order of milliseconds), such as with small molecule surfactants, it is necessary to resort to other techniques to measure the dynamic surface stress.

Maximum bubble pressure method

Transient changes in interfacial stress due to the surface and bulk diffusion of surfactants dictates film drainage [161], ultimately influencing the stability of foams and emulsions. The maximum bubble pressure method is an appropriate technique for characterizing these important transient changes in surface stress at high frequencies [160, 162, 163], and can be conveniently performed in single bubble/drop setups. The method involves bubbling a fluid through a capillary and measuring the pressure as a function of the bubbling frequency. The capillary pressure reaches a maximum when the radius of curvature of the bubble/drop equals the radius of the capillary. Utilizing this information, an isotropic surface stress is recovered from the simplified Young-Laplace equation as below,

$$\sigma_{\alpha\beta}(\Gamma(t_{max})) = \frac{aP_{cmax}}{2} f_c \tag{23}$$

Here, a is the radius of the capillary, f_c is a shape correction factor that accounts for any deviation of the bubble from a spherical shape, P_{cmax} is the maximum capillary pressure and t_{max} is the time taken for attaining P_{cmax} after forming a new bubble/drop (equivalently after releasing a bubble/drop). P_{cmax} is obtained by subtracting the hydrostatic pressure (P_h) and the excess dynamic pressure P_d from the pressure P_t measured by the pressure transducer, i.e $P_{cmax} = P_t - P_h - P_d$. To obtain the surface stress as a function of the interface age, t_{max} is varied by changing the bubbling frequency. Additional details about the technique including the calculation of f_c and P_d, considerations for very high frequency measurements, and the dilatational contributions to the measured surface stress are available in Fainerman et al. [162].

Microscopic drops

"Microtensiometers" are commonly used to measure the dynamic interfacial stress of microscopic spherical drops with radii of curvature on the order of $10 - 100$ μm [136, 137, 164–168]. Being able to measure the dynamic interfacial stress of micron-scale systems provides a great advantage to the study of foams and emulsions, since the characteristic sizes of these systems typically range on the order of $10 - 100$ μm [133].

In these devices, a small spherical drop or bubble with Bo $\ll 0.01$ is created at the tip of a capillary, which is itself connected to a pressure transducer [136, 164, 165]. Fluid is delivered to the tip of the capillary to create a drop/bubble, which is imaged using a magnified objective connected to either a regular or a high speed camera. The volume of the drop or bubble is controlled either directly, using a syringe pump, or indirectly, by adjusting the internal pressure of the drop/bubble via an external pressure head [136, 164, 168–170].

The dynamic surface tension for a simple interface $\sigma_{\alpha\beta}(\Gamma(t))$ can be determined from direct measurements of the pressure jump across the interface and the radius of the

drop/bubble [136, 164, 165]. Since Bo $\ll 0.01$, the hydrostatic pressure contribution can be neglected and Eq. 19 can be simplified to obtain the Young-Laplace equation for a spherical interface with a radius of curvature equal to R_a:

$$\Delta P_a = \frac{2\sigma_{\alpha\beta}(\Gamma(t))}{R_a}. \tag{24}$$

This same technique can also be used to determine the isotropic dynamic interfacial stress of a static, undeformed complex interface.

Microtensiometry presents an advantage over other macroscopic techniques, which employ drops with radii of curvature on the order of millimeters, due to the faster adsorption times [165]. The use of micron-scale drops and bubbles not only requires smaller solution volumes than traditional methods, but also reduces the time required for an interface to reach its equilibrium configuration by almost an order of magnitude because the time scale for molecular diffusion is dependent on the radius of curvature of the interface, and is thus smaller for a convex curved interface compared to its planar counterpart [135, 165].

As reported by Alvarez et al., the dynamic interfacial tension of large macromolecules (such as proteins and polymers) can be determined on the order of minutes or hours rather than days, as required with pendant drop tensiometry [136, 165]. Furthermore, due to the smallness of the drops, high speed cameras with narrow fields of view can be used at frame rates upwards of 10,000 frames/s, which also allows this technique to be used to accurately study the adsorption dynamics of smaller molecules [164].

Microtensiometry also allows the user to determine whether the transport dynamics are governed by species diffusion or adsorption kinetics [136, 165, 171]. Surfactant transport to an initially clean interface is governed by three simultaneous transport processes: (1) diffusion of surfactant dissolved in the bulk towards the fluid/fluid interface, (2) adsorption/desorption at the interface due to entropic effects, and (3) reorientation and reconfiguration of the adsorbed surfactant due to enthalpic effects [136, 165]. Since diffusion is a function of the interfacial curvature, the dependence of the dynamic interfacial stress on the drop radius can be used to elucidate whether, at a particular bulk concentration and size, the transport dynamics diffusion limited [165].

Microfluidic methods, which require the use of a convective bulk flow, have also been developed to measure interfacial stress at micron-scale interfaces. Additional details on this technique can be found in references [172, 173].

3.4.2. Dilatational rheology

The dilatational rheology of complex fluid-fluid interfaces is correlated to the stability and lifetime of foams and emulsions [136]. Understanding how complex fluid-fluid interfaces respond to area-changing deformations can also provide further insight to processes involving droplet break-up, nucleation, and coalescence. Dilatational deformations can be achieved using the drop/bubble setups outlined in the previous section. By changing the internal volume of a drop or bubble, the interface can be compressed or dilated either in a single step-wise manner or in a continuous oscillatory fashion.

Step-strain

During a step-strain measurement, a pendant bubble or drop is rapidly compressed/expanded by withdrawing/infusing fluid from it using a syringe pump [134, 140, 141]. This technique can be carried out with spherical or non-spherical geometries, and requires the use of the pendant bubble/drop setup for complex interfaces described in ***Section 3.4.1***. Changes in the interfacial stress and drop geometry are measured as the drop/bubble is allowed to relax back to an equilibrium configuration [134, 140, 141]. Thus, step-strain experiments can be carried out using large areal strain deformations within the non-linear regime that improve the signal-to-noise ratio in the pressure transducer output and decrease the relative error in the drop area change calculations [134].

Step-strain experiments consist of three steps: interface aging, step-strain compression/expansion, and stress relaxation [133]. During the first step, a syringe pump is used to form a drop/bubble at the tip of a capillary, which is submerged in the bulk fluid. The initial drop/bubble shape can either be spherical [46, 130, 133] or non-spherical [134, 141, 174]. Spherical geometries are preferred when different compositions and interfacial tensions are being compared, as it is important to maintain a constant initial volume and surface area for all systems since experiments are often conducted within the nonlinear viscoelastic regime [133].

Once the drop is formed, the system is allowed to age for the desired aging time. After aging is complete, a step-strain compression/expansion is applied to the drop by using a syringe pump to withdraw/inject fluid until the final volume is reached. The applied flow rate can be thought of as analogous to a strain rate. Thus, step-strain experiments can be conducted by varying the interface aging time and/or the compressional strain rate [133]. Once the drop reaches its final volume, it is allowed to relax back to an equilibrium shape and pressure. A time-dependent compressional relaxation modulus is calculated during this step [46, 130, 133].

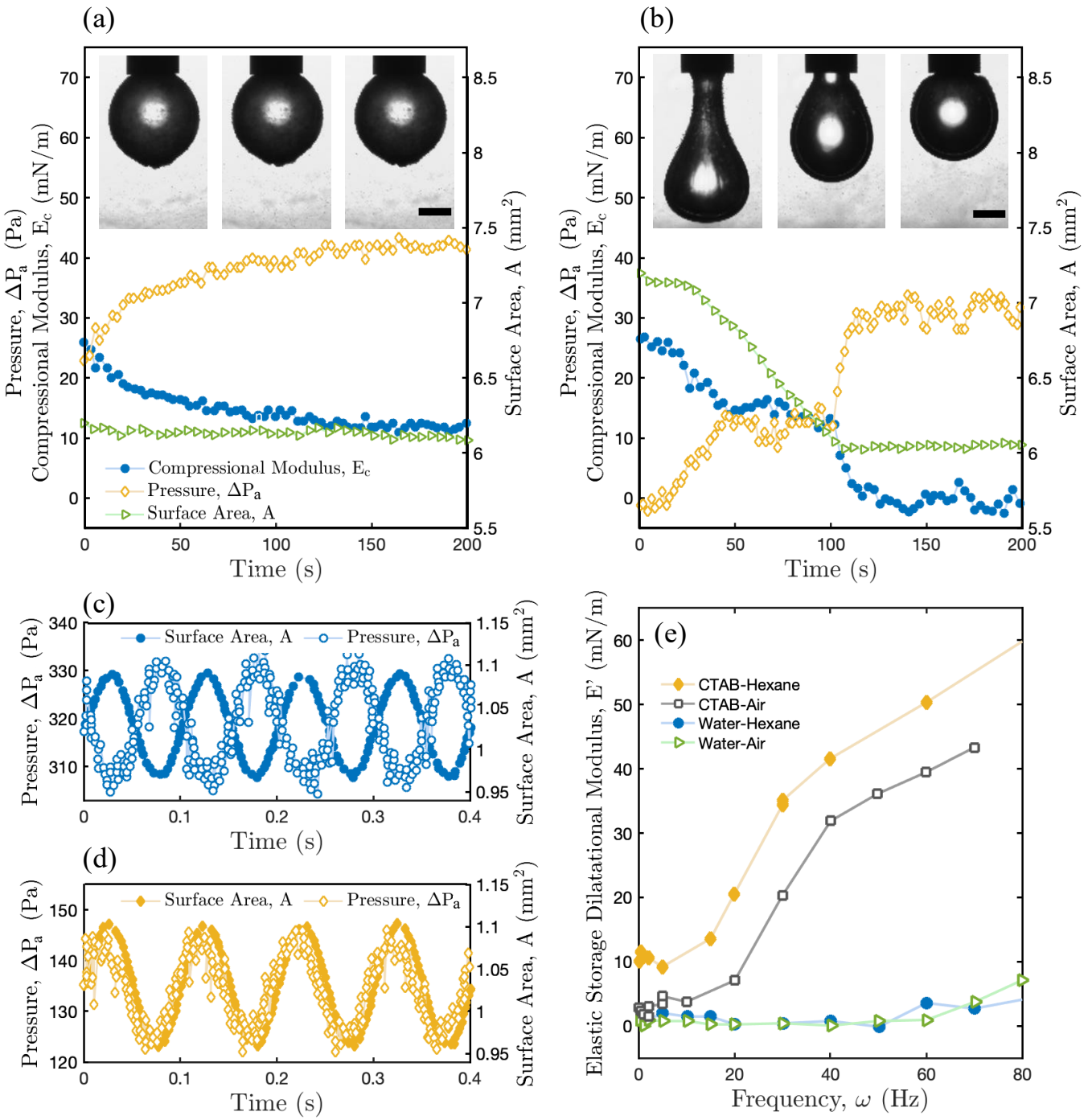

Figure 7: Top: Compressional step-strain relaxation profiles for a pendant water drop suspended in a 1 mg/mL asphaltene in toluene solution (**a.**) or a 1 mg/mL asphaltene + 2 % polymer in toluene solution (**b.**). The drops are aged for 60 min and compressed at a flow rate of 0.1 µL/s. Snapshots are shown at 0, 100, and 200 s after stress relaxation begins (scale bar = 0.5 mm). Asphaltene-only interfaces show a time-dependent pressure relaxation but no shape change upon compression, whereas the polymer-laden system shows both a shape and a pressure relaxation. Results reproduced from Rodriguez-Hakim et al. [133]. Bottom: Surface area and Laplace pressure during small amplitude oscillations of a spherical drop of pure water (**c.**) and a drop of aqueous 0.1 mM CTAB solution (**d.**) in hexane (frequency = 10 Hz). The in-phase component of the oscillations is used to calculate the storage elastic modulus, E', for different water and CTAB interfaces. (**e.**) Water-hexane interfaces are non-viscoelastic (phase shift $= \pi$ and $E' = 0$) and CTAB-hexane interfaces exhibit a predominant elastic response (phase shift $< \pi/2$). Results reproduced from Javadi et al. [164].

Since step-strain dilatational rheology allows the use of non-spherical geometries, the measured interfacial stress can adopt a non-isotropic form as outlined in ***Section 3.4***. Depending on whether the measured stress is a scalar or a tensor, a time-dependent scalar or tensorial dilatational modulus can then calculated from the drop's surface area, radius, and the Laplace pressure jump across the apex, as follows [46, 130, 133],

$$\boldsymbol{E}(t) = \frac{\Delta\boldsymbol{\sigma}(t)}{\Delta A/A_i} = \frac{\boldsymbol{\sigma}_i - \boldsymbol{\sigma}(t)}{(A_i - A(t))/A_i}. \tag{25}$$

Here, $\boldsymbol{\sigma}_i$ and A_i are the interfacial stress tensor and surface area before the step-strain deformation, and $\boldsymbol{\sigma}(t)$ and $A(t)$ are the time-dependent values during relaxation.

Fig. 7(a-b) shows an example of different stress relaxation profiles that can be obtained with different complex interfaces, reproduced from Rodriguez-Hakim et al. [133]. In this example, the drop phase is composed of DI water and the bulk phase is a 1 mg/mL asphaltene in toluene solution without (Fig. 7a) or with (Fig. 7b) the addition of a surface active co-polymer at 2 wt%. The results shown correspond to an interface aging time of 60 min and a compressional flow rate of 0.1 µL/s. The plots show the time evolution of the surface area A, apical Laplace pressure jump ΔP_a, and apical compressional modulus E_c during the relaxation step. Asphaltene-only interfaces show a time-dependent pressure relaxation but no shape change upon compression, whereas the polymer-laden system shows both a shape and a pressure relaxation. To simplify the analysis, the spatial dependence of the modulus was removed by only calculating the modulus value at the drop apex, where spherical symmetry holds and the elastic stresses are locally isotropic (i.e. $\sigma_s = \sigma_\phi$, as seen in Fig. 6) [133, 134, 141].

Despite the differences in the temporal behavior of $E(t)$, two important parameters can be extracted from the curves: the initial compressional relaxation modulus $E_c(t = 0)$ and the static (or equilibrium) compressional relaxation modulus, $E_c(t \to \infty)$ [46, 130, 133]. $E_c(t = 0)$ represents the accumulation of elastic energy at the onset of compression [46, 130, 133] and $E_c(t \to \infty)$ is the long-time equilibrium value of the surface elastic energy. Physically, it represents the degree of irreversibility of the film, or its solid-like character [46]. The lower $E_c(t \to \infty)$ is, the better the interface is at dissipating the accumulated elastic energy [46, 130, 133]. If $E_c(t \to \infty)$ is finite, as in Fig. 7a, the adsorbed species is irreversibly adsorbed onto the interface, forming a highly solid network that is associated with the long-term stability of emulsions.

Oscillatory

In oscillatory dilatational rheology, a sinusoidal change in the bubble/drop's surface area [164] or pressure [168] is imposed via the injection and withdrawal of fluid. This technique requires the use of spherical drops or bubbles and is carried out using the microtensiometer setup outlined in ***Section 3.4.1*** or similar capillary pressure tensiometers [164, 165, 168–170]. The drop/bubble is formed and remains undisturbed until adsorption equilibrium is established at the fluid/fluid interface [164]. The interface is subjected to infinitesimal strain amplitudes, where the change in surface area, $\Delta A \lesssim 10$ % [164]. This is particularly important for complex interfaces in order to ensure that a spherical geometry is maintained at all times. A pressure transducer is coupled to the capillary setup that allows for a simultaneous measurement of the surface area and internal pressure of the drop [136, 164, 165, 171]. Measurement of the drop/bubble radius and internal pressure are sufficient to calculate the oscillatory dilatational moduli [136, 164, 165, 171].

The dilatational modulus of an oscillating drop/bubble exhibits two contributions: an elastic part that represents the recoverable, or stored, energy of the interface (captured by the surface storage modulus, E') and a viscous part that represents the dissipated energy (captured by the surface dilatational loss modulus, E'') [136, 164, 171, 175]. E' and E'' correspond to the real and imaginary parts of the complex surface dilatational modulus, E^*, where $E^* = E' + \mathrm{i}E''$ [136, 164, 171, 175]. The moduli values are functions of the oscillation frequency ω; thus,

$$E^*(\omega) = \frac{\Delta\sigma}{\Delta A/A(t=0)} e^{i\Phi(\omega)}, \tag{26}$$

$$E'(\omega) = \frac{\Delta\sigma}{\Delta A/A(t=0)} \cos\Phi, \tag{27}$$

$$E''(\omega) = \frac{\Delta\sigma}{\Delta A/A(t=0)} \sin\Phi, \tag{28}$$

where Φ is the phase angle difference between the applied strain and the measured stress, $A(t = 0)$ is the reference (initial) surface area, ΔA is the amplitude of the surface area strain, and $\Delta\sigma$ is the amplitude of the interfacial stress change [136, 171, 175]. Since the drops remain spherical at all times for small strain deformations, the interfacial stress remains isotropic even for complex interfaces (recall that for drops/bubbles with isotropic stress distributions, $\boldsymbol{\sigma}$ can be expressed as $\boldsymbol{\sigma} = \sigma \boldsymbol{I}_s$). Thus, for a constant radius of curvature, negligible gravitational effects (i.e Bo ≤ 0.01), and a spatially constant interfacial stress, the expression for σ is given by Eq. 24, where $\sigma = P_a R_a/2$.

Fig. 7(c-e) reproduces results obtained by Javadi et al.

for simple and complex interfaces [164]. Parts (c-d) of the figure show plots of the Laplace pressure jump ΔP_a and the surface area A during oscillatory dilatational experiments with spherical drops composed of either pure water or a 0.1 mM aqueous CTAB solution, respectively, in contact with a bulk hexane phase. This data can be used to compute the surface storage and loss moduli, E' and E'', using Eqs. 24, 27, and 28. E' is plotted in Fig. 7e for different drop and bulk compositions. The surface area and pressure oscillations in Fig. 7c for a pure water drop in hexane are completely out of phase (i.e a phase shift of π), since the water-hexane interface is simple and non-viscoelastic. As seen in Fig. 7e, simple interfaces such as water-hexane and water-air have moduli of zero. When CTAB adsorbs onto the water-hexane interface, it renders the interface viscoelastic (Fig. 7(d-e)). Since the oscillations in A and ΔP_a are almost in phase, the interface has a predominant elastic character. Analogous results are seen for CTAB-air interfaces.

Due to geometric constraints, small amplitude oscillatory interfacial dilatational rheology is capable of determining the interfacial dilatational moduli for both simple and complex interfaces. It is also possible to conduct a frequency sweep by varying the oscillation frequency ω in order to see where the crossover between an elastic-dominated and a viscous-dominated response occurs [136, 175].

This method has several limitations. Infinitesimal area strains are required, which may make it difficult to obtain accurate pressure readings from the transducer [135]. Gas compressibility effects can also introduce spurious phase differences between the applied strain and the measured stress [72]. Further, it is required that the pressure, stress, and area oscillations remain sinusoidal at all times, where the effect of higher order harmonics is mitigated [135, 136]. The magnitude of higher harmonics can be determined via a Fourier analysis of the oscillatory radius and pressure data [136, 176]. Kotula et al. specify an acceptable experimental criterion where the harmonic ratio (i.e the ratio of the second vs the first order harmonics) should be less than 0.1 [136].

In addition, the interfacial stress is computed using the Young-Laplace equation for a static interface, so it is assumed that the shape of the drop is in equilibrium at all times. This requires a slow, quasi-steady change in the drop shape, such that the capillary and Reynolds numbers are small [135, 136]. The capillary number, Ca, measures the relative contribution of viscous stresses arising from interfacial motion (where the drop/bubble apex translates a vertical distance Δd during the period of an oscillation) versus dilatational stresses [136]. The Reynolds number, Re, prescribes the relative importance between inertial and viscous stresses, where significant fluid inertia can cause additional pressure jumps across the interface [136]. The operating dimensionless parameters for oscillatory interfacial dilatational rheology are summarized below, and a further discussion of the operating ranges can be found in Kotula et al. [136]

$$\mathrm{Bo} = \frac{\Delta \rho g R_a^2}{\sigma} \leq 10^{-2}, \tag{29}$$

$$\mathrm{Ca} = \frac{\mu \omega \Delta d}{\sigma} \leq 10^{-6}, \tag{30}$$

$$\mathrm{Re} = \frac{\rho \omega R_a \Delta d}{\mu} \leq 10^{-1}. \tag{31}$$

4. Foam stability

In this section we will discuss the recent developments in bubble and foam stability science facilitated by single bubble methods.

4.1. Foam Density

Foam density, also referred to as the liquid fraction [3, 177], foam wetness [178], or quality, [179] is a measure of the amount of liquid entrained in the foam [71]. Foam density is an important characteristic that has consequences for many industries such as food [6], froth flotation and extraction [179, 180], and the lubricant industry [181]. Traditionally, mechanistic studies on foam density are usually performed using bulk foam tests such as the foam rise test [180, 181]. Recently, Frostad et al. [71] have shown that single bubble experiments are a convenient platform to obtain mechanistic insights into foam density by establishing a correlation between the mean film thickness measured from single bubble experiments and the foam density measured from bulk foam experiments (Fig. 8a). Subsequently, the same technique has been used by a number of researchers to probe the effects of interfacial properties on foam density [47, 131].

We will discuss two notable developments. Firstly, experiments by Frostad et al. [71] have revealed the nuances in the role of Marangoni stresses in controlling foam density across different types of surfactants. As seen in (Fig. 8a), at about 2 mM concentration, the foam density in solutions with the surfactant CTAB crosses over the foam density of solutions with the surfactant Triton. This is very surprising as the surface tension of Triton is always lower than CTAB at a similar concentration. A closer look at the evolution of the mean film thickness measured over single bubbles shows that despite trapping a thicker film as expected, bubbles in Triton solutions drain faster than in SDS solutions (Fig.8 b). Even though the precise reason for this behavior is unknown, the relatively enhanced terminal drainage of Triton explains its lower foam density despite being capable

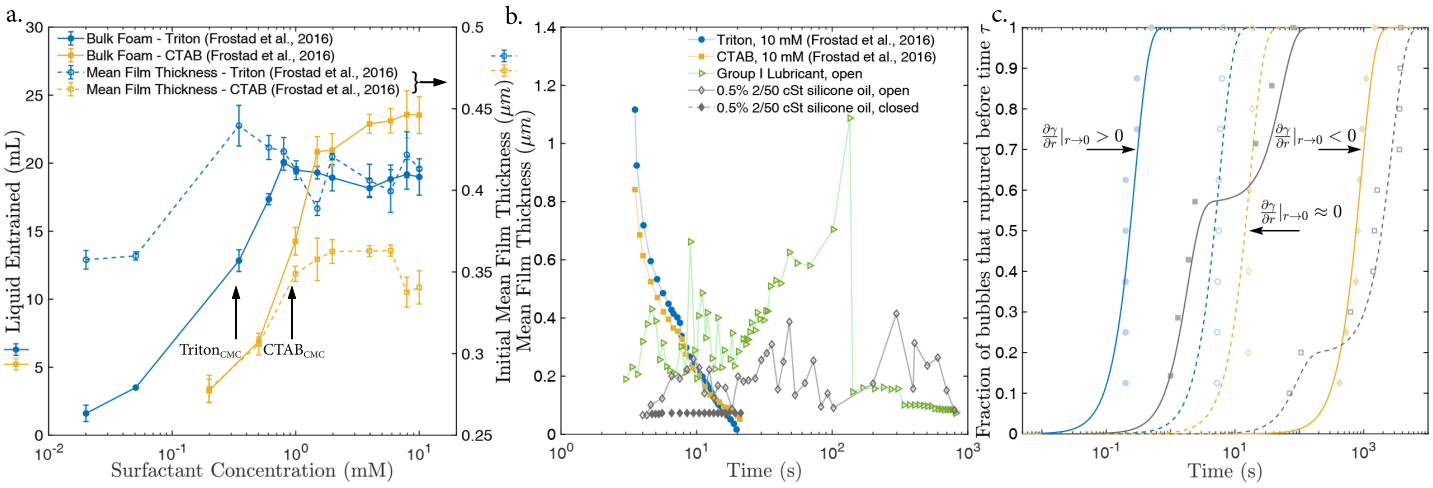

Figure 8: Insights into foam stability from single bubble measurements. (**a.**) Demonstration of the positive correlation between bulk foam density and initial mean film thickness obtained from single bubble experiments as a function of surfactant concentration. Solid lines correspond to foam density measured from a foam rise test immediately after cutting of air injection, while the dashed lines correspond to the mean film thickness measured from single bubble experiments immediately after the bubble comes to rest at the air-liquid interface. Data obtained from Frostad et al. [71]. (**b.**) Evolution of the mean film thickness, $\bar{h} = (\pi R_0^2)^{-1} \iint h(r,\theta) r dr d\theta$ (see Fig. 1 for definition of the variables). The Triton and CTAB data are reproduced from Frostad et al. [71], while the Group I lubricant and silicone oil mixture data are reproduced from Suja et al. [8]. (**c.**) Coalescence time distributions showing bubble stability in different systems. ● 10% Toluene in 50 cSt silicone oil (open), ○ 10% Toluene in 50 cSt silicone oil (closed), ♦ 0.5% 2 cSt in 50 cSt silicone oil (open), ◇ 0.5% 2 cSt in 50 cSt silicone oil (closed), ■ 10 μm filtered lubricant, □ 1 μm filtered lubricant. The silicone data is reproduced from Suja et al. [73], while the lubricant data is reproduced from Suja et al. [9]. The silicone data shows the influence of the radial direction of Marangoni stresses on bubble stability, while the lubricant data shows the effect of the pore size of filters on bubble stability in filtered lubricants with antifoams.

of trapping a thicker film by generating larger Marangoni stresses. Secondly, experiments by Lin et al. [131] and Kannan et al. [47] have presented a better understanding of the role of interfacial shear elasticity on the entrained film volume. There exist contradicting conclusions on the effects of interfacial elasticity, with some studies correlating higher interfacial shear elasticity with higher entrained film volume while others finding no such correlation [131]. A resolution to these contradictions was presented by Kannan et al. [47] by arguing that film drainage rates saturate above some critical value of the elastic modulus and that differences in film drainage can be perceived at lower values of the elastic modulus. Similar effects were reported for the film drainage as a function of interfacial viscosity of Newtonian interfaces. For films draining over solid domes, Bhamla et al. [182] observed an almost 100% reduction in the drainage rate for a 10-fold increase in the Boussinesq number from a value of 1 (non-dimensional number proportional to the interfacial viscosity), while no significant changes in drainage were observed for a further increase in the Boussinesq number beyond a value of 10. Both the above observations are most likely a result of the interface behaving as a no-slip surface above sufficiently high values of the interfacial modulus.

4.2. Coalescence time distributions

As single bubble coalescence times are inherently stochastic, quantifying and comparing bubble coalescence times to bulk foam stability requires the use of appropriate statistical tools [92, 97, 99]. One such tool is the coalescence time distribution (see Fig. 8c and ***Section 3.2***). Notable developments in this area are mentioned below.

Firstly, recent results have shown that coalescence time distributions can be conveniently used to rank non-aqueous foam stability [8]. This is accomplished by constructing a series of distributions (eg. see coalescence times fit to Rayleigh distributions for silicone oil mixtures in Fig.8c), and inferring the relative position of the distributions. The farther right the distribution falls along the time axis, the more stable are the bubbles and consequently the more stable is the foam. The rationale for the varying foam stability in the silicone mixtures observed in Fig.8c is discussed in ***Section 4.3***.

Secondly, coalescence time distributions have been shown to be sensitive to the presence of antifoams [9]. Coalescence times of naturally rupturing (without antifoams) bubbles are known to described by a single Weibull type distribution. However, in the presence of antifoams, we observe that bubble coalescence times are better described by mixture distributions (Fig.8c). This is not surprising as the coales-

cence time of a bubble is dependent on whether a bubble encounters an antifoam or not, with bubbles rupturing relatively quickly when antifoams are present. As a result, the measured coalescence times can fall under two different distributions with different means depending on the presence of antifoams. Further, the size of the antifoams also influence the coalescence time, with larger antifoams lowering the coalescence time. Both these effects can be seen in the coalescence time distributions (fit to Rayleigh distributions) of bubbles in antifoam-laden lubricants filtered using a 1 μm and 10 μm filter (Fig.8c). In the 1 μm filtered lubricant, as a result of the very small filter pore size, the majority of the antifoam particles have been filtered out. Consequently a significant portion of the bubbles (those above the shoulder) never encounter an antifoam and remain stable for a longer time. On the other hand, in the 10 μm filtered lubricant, all bubbles encounter antifoams. However, due to a distribution of antifoam sizes in the lubricant, we again observe a mixture distribution. The means of the two distributions are most likely set by the two dominant antifoam sizes in the lubricant, with the distribution above the shoulder corresponding to bubbles ruptured by the smaller antifoam. Currently, efforts are underway to correlate the scale parameters and mixture ratios of the underlying Rayleigh distributions to the dominant antifoam sizes and their number densities [9].

As a concluding note, we highlight that the results presented in Fig. 8c are for liquid antifoam droplets obeying the so called Garett's hypothesis [3, 183]. It would be worthwhile for future studies to investigate antifoams that do not adhere to the Garett's hypothesis and establish their influence on the coalescence time distributions.

4.3. Stabilization Mechanisms

Single bubble experiments have played an important role in uncovering and mechanistically understanding foam stabilization mechanisms. A number of prior reviews have summarized the effects of interfacial rheology and traditional surfactant mediated Marangoni stresses in stabilizing bubbles [31, 44, 184]. In this section we will focus only on the previously unreported mechanisms. Notable examples are presented below.

Bubble stabilization by evaporation induced Marangoni flows has been the subject of a number of recent studies. Evaporation can drive Marangoni flows through changes in temperature as well as through changes in species concentration. The former, commonly referred to as thermocapillary Marangoni flows, is known to dictate bubble stability in highly volatile liquids with low specific heats [79]. The later, commonly referred to as solutocapillary Marangoni flows [118], is known to alter the stability of bubbles in liquid mixtures with at least one volatile component. Evaporation driven solutocapillary Marangoni flows are known to increase bubble lifetimes in alcohol-water mixtures [185, 186]. Interestingly, recent studies have revealed the important effect of solutocapillary flows on the stability of bubbles in non-aqueous systems such as lubricants [8, 73].

As shown in Fig. 8c using mixtures of silicone oils, bubble stability depends on the radial direction of the Marangoni stresses induced by evaporation. Bubbles are stabilized when the Marangoni stresses compete against capillary flows and drive fluid to the bubble apex, while bubbles are destabilized when Marangoni stresses drive fluid away from the bubble apex. An interesting signature of the former case is the spontaneous cyclic dimple formation and dissipation resulting from the competition of Marangoni flows that drive fluid to the apex of the bubble and capillary flows that thin down the film [8, 187, 188]. As a result, dramatic fluctuations are observed in the film thickness of bubbles, along with a marked increase in their life time (see the data for a Group I lubricant and a silicone oil mixture in Fig.8b). When evaporation is suppressed, for instance by sealing the system, capillary forces steadily drain the film without competition and no fluctuations are observed. As expected, for closed systems, bubble stability decreases if evaporation is stabilizing and vice versa (Fig. 8c).

4.4. Bubble rupture dynamics

Single bubble experiments have also played a pivotal role in establishing the rupture dynamics of bubbles. Good discussions on hole opening kinetics [189–191], topological changes [189, 191, 192], and fragmentation dynamics [99, 190] are available in the literature. Here we will briefly comment on the recent developments in this area.

Firstly, recent studies have revealed the influence of bulk elasticity in the hole opening kinetics of bubbles in a number of systems such as Boger fluids [193], wormlike micelles [194], and polymer melts [195]. In all cases, at short times, bulk elasticity was revealed to increase the hole opening velocity by as much as 10^4 times as compared to a Newtonian fluid of similar viscosity. This is expected as the elastic stresses that build up during bubble formation aid the capillary stresses in rupturing the bubble, leading to an increase in the rupture velocity.

Secondly, recent research has also improved our understanding of the topology of bubbles during rupture. Notably, Debrégeas et al. [195] have shown that during rupture, buckling instabilities can occur on the surface of bubbles in polymer melts. Sabadini et al., [194] on the other hand, have interestingly reported a complete absence of a rim (the tip of the expanding hole where liquid accumulates) in bubbles rupturing in viscoelastic wormlike micellar solutions. The reason for this is currently unknown.

Thirdly, a number of studies have focused on fragmentation dynamics [99, 196]. The retracting fluid at the rim is known to fragment via a sequence of hydrodynamic instabilities, namely a Rayleigh-Taylor instability generating the ligaments at the bubble rim followed by a Rayleigh-Plateau instability generating droplets from the ligaments. For bubbles in simple liquids, the mean size of these generated droplets $\langle d \rangle$ was shown by Lhuissier and Villermaux to scale with the mean thickness of the film $\bar{h}$ (see Fig.8 caption for the mathematical definition of $\bar{h}$) as $\langle d \rangle \sim \bar{h}^{5/8}$, and from mass conservation, the number of drops N to scale as $N \sim \bar{h}^{-7/8}$. Building on this result, Poulain et al. [196] have shown that bacterial secretions reduce the size and increase the number of droplets released during bubble rupture by lowering the film thickness at rupture. As a result, these pathogens spread more readily by taking advantage of the mechanics of bubble rupture. In the future, it would be worthwhile for studies to further investigate the impact of interfacial properties, especially the effects of interfacial rheology, on the dynamics of bubble rupture [197].

5. Emulsion stability

The physical mechanisms governing the stability of an emulsion are not yet fully understood, but there exist a number of theories confirmed by experiments that have shed light on this problem for over more than a century. In this section we present some of the most relevant and established models dealing with emulsion stability and coalescence, as well as more recent advances and potential developments of the single drop techniques.

5.1. Stabilization mechanisms and film rupture

A stable emulsion can be formed under some conditions, and by means of different physical mechanisms. The most common procedure to increase the stability of emulsions is the addition of surface active species in sufficient quantity to form dense surface layers [199]. Stable thin films of constant thickness can then be formed, preventing adjacent droplets from coalescing. In particular, it was proposed [200] and experimentally demonstrated [201] that the added surfactant must be soluble in the continuous phase and insoluble in the disperse phase in order to optimize the increase in stability. The relevant stabilization mechanism is the well known Marangoni flow: when two droplets approach and come into contact (or a droplet and a planar interface), surfactant molecules are driven towards the film perimeter, creating gradients in surface concentration, and in turn, surface tension gradients. When the surfactant is soluble in the disperse phase, there is a source of surfactant molecules to rapidly replenish the surface, eliminating the surface tension gradients. Hence, Marangoni flows are suppressed and the film thins faster. On the contrary, when the surfactant is soluble only in the continuous phase and the film is thin enough, there are not enough surfactant molecules available to replenish the surface. Hence, Marangoni flows that oppose the film thinning are sustained, and the film thins at a slower rate [199].

In general, ionic surfactants are more efficient in stabilizing emulsions. An intuitive explanation of this observation is given in Fig. 9a, where we represent the disjoining pressure, π_d, versus the film thickness when a monolayer of an ionic surfactant is present in both interfaces [125, 199, 202]. At large film thicknesses, the interaction between the interfaces is governed by the addition of electrostatic repulsion (screened-Coulomb or Yukawa potential) and van der Waals attraction, known as DLVO (Derjaguin-Landau-Verwey-Overbeek) forces. At much smaller film thicknesses, short range forces govern the dynamics. If the pressure in the thin film is smaller than the local maximum of the disjoining pressure represented in Fig. 9a by a red circle (π_d^*), the film would thin until it reaches an equilibrium value of the order of hundreds of nanometers. If the pressure is higher, the equilibrium thickness is much smaller, where the fluid separating the monolayers has been fully removed and a bilayer is formed.

It is well known that solid particles located on the liquid/liquid interface can increase emulsion stability, forming the so-called Pickering emulsions [203]. There exists strong evidence that the physical mechanism arresting coalescence in Pickering emulsions is the formation of a steric barrier by the particles [204–208]. This mechanism requires the adsorption of the particles at the interface, which is possible only when the three phase contact angle is close to 90°. Hence, the amphiphilic character of the particles facilitates the stabilization of the emulsion. The main application of Pickering emulsions, extensively used in the last decades, is the fabrication of nanomaterials such as microspheres and microcapsules, with direct applications in the food or pharmaceutical industries [209–211]. For a review on Pickering emulsions focused on the different types of emulsifying particles and the nanomaterials fabricated from Pickering emulsions, the reader is addressed to Yang et al. [208].

In spite of the fact that the coalescence process is not fully understood, the physical mechanisms leading to the apparition and eventual nucleation of a hole in the thin film have been examined for decades. De Vries [198] studied the energetics of hole nucleation, finding that there exists a critical hole size below which hole growth is energetically unfavorable. This theory is based on the calculation of the increment in surface area associated with the hole growth, where there is both a loss in surface area given by $2\pi r^2$

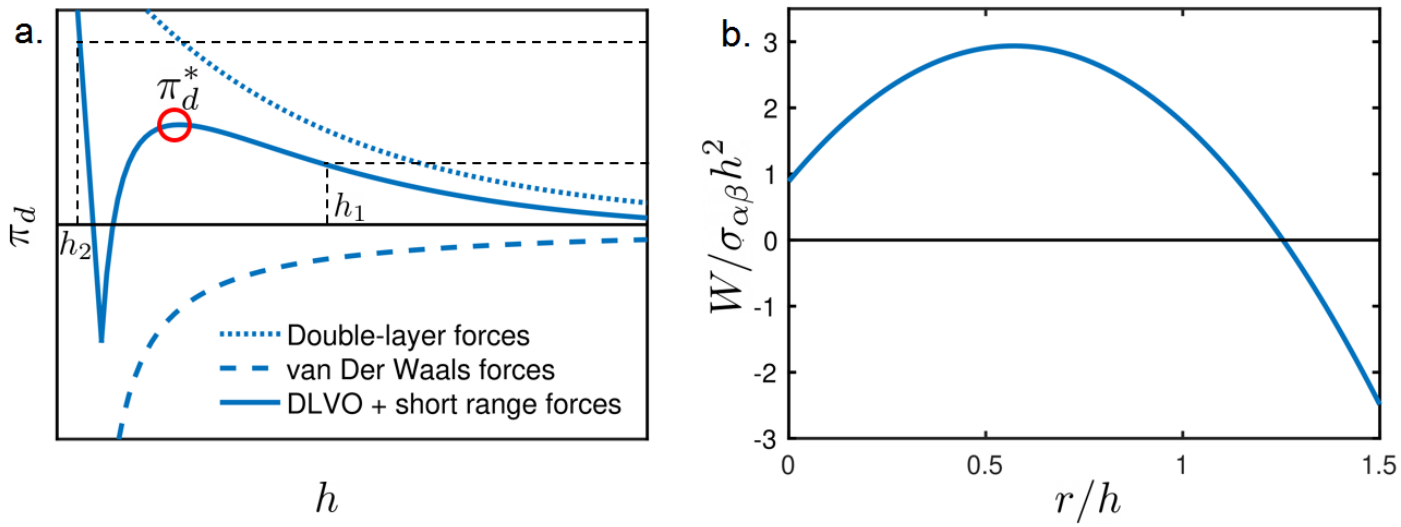

Figure 9: (**a.**) Disjoining pressure versus film thickness h, where the dotted curve represent the double-layer forces (the electrostatic -repulsive- contribution) and the dashed curve represents the van Der Waals forces (attractive). The solid curve represents the addition of these two contributions (DLVO forces) plus the short range forces. If the pressure in the thin film is smaller than the local maximum, π_d^*, DLVO fores dominate and the equilibrium thickness h is of the order of hundreds of nm (h_1). If the pressure is bigger than π_d^*, h is much smaller (of the order of a few nm, h_2), short range forces dominate and, essentially, the two interfaces form a bilayer. (**b.**) Non-dimensional free energy of the nucleated hole as a function of its non-dimensional size, calculated from the de Vries theory [198]. The hole nucleation is energetically unfavourable until a critical r/h value is reached (about 0.5). Here r is the radius of the hole, h is the film thickness, W is the free energy, and $\sigma_{\alpha\beta}$ is the interfacial tension. The hole spontaneously increases in radius once that critical value is exceeded.

(where r is the radius of the hole) and an increase in surface area due to the formation of a hole rim. Assuming that the hole rim is perfectly circular and the surface tension is uniform, the resulting non-dimensional free energy of the nucleated hole as a function of its non-dimensional size is represented in Fig. 9b, where the free energy, W, has been made dimensionless by $\sigma_{\alpha\beta}h^2$, $\sigma_{\alpha\beta}$ being the interfacial tension and h the thin film thickness.

Other models have been proposed [212], accounting, for instance, for the spontaneous curvature of the surfactant molecules [95, 213]. However, all these models predict an activation energy orders of magnitude higher than k_BT for the typical values of the equilibrium thickness ($\sim 100\,\text{nm}$). Therefore, a reasonable coalescence mechanism for emulsions stabilized by ionic surfactants is as follows [199]: the local maximum in Fig.9a arising from the electrostatic potential is decreased due to surface concentration fluctuations, allowing the film to locally thin to a much smaller thickness, where short range forces dominate the dynamics. The activation energy is not much larger than k_BT now, such that hole nucleation is possible. Following the nomenclature by de Gennes [214], this mechanism represents the classical view of *intrinsic* coalescence. However, in many applications, the most favorable coalescence mechanism is different in nature: analogous to the effect of antifoams discussed in ***Section 4.2***, a particle located in the thin film separating two droplets can bridge the film and facilitate coalescence, producing the so-called *extrinsic* coalescence.

5.2. Single drop experimental approach

As explained in ***Section 3***, the experimental setup for single drop and single bubble experiments is essentially identical. Moreover, the main observables are coalescence times and interferometric images in both cases. Since the experimental details and the fundamental details of coalescence time distributions and film thickness reconstruction have already been discussed in the preceding sections, we will confine ourselves to present some recent results to highlight the applicability of the technique to the emulsion problem. At the end of this section, we will examine the film rupture dynamics in the case of emulsions, discussing the potential application of single drop techniques to this question.

5.2.1. Coalescence time distribution and drainage rate

A number of studies utilizing single drop setups have improved our understanding of the influence of surfactant type and surfactant concentration[88], phase viscosity ratio [90] and drop size [87] on drop coalescence times. In particular, recent studies by Basheva et al.[87] and Politova et al.[88], have shown that buoyancy induced drop coalescence lifetimes are non-monotonically related to drop size,

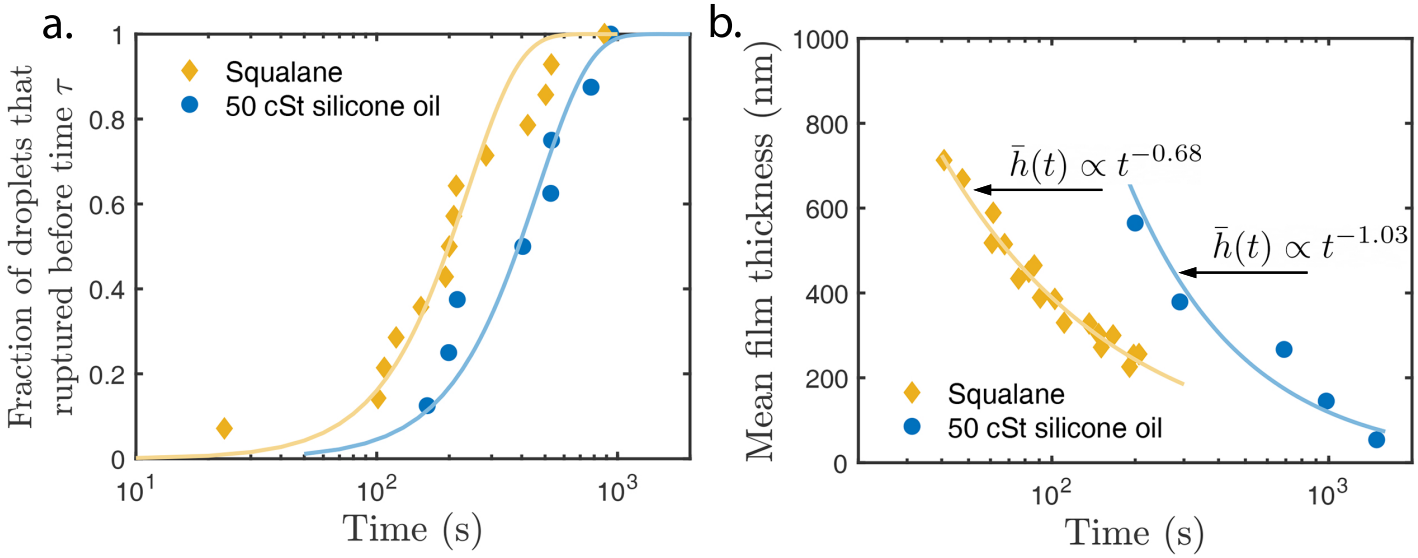

Figure 10: (**a.**) Coalescence time distributions of oil droplets against a flat oil/water interface. The symbols represent the experimental data, and the curves show the corresponding Rayleigh distributions. (**b.**) Mean film thickness ($\bar{h}$) versus time for the same two samples. The curves show the best fit to a function of the form $\bar{h}(t) \propto t^{-\xi}$ where the the best fit values for $-\xi$ are -1.03 and -0.68 for the silicone oil and the squalane, respectively.

with long lifetimes for very small and large drops. This has been shown to be a consequence of finite drop deformation above a critical size, which retards coalescence by trapping a thicker film [161].

The stability of deleterious lubricant-water emulsions were also recently investigated. Fig.10a shows coalescence time distributions for squalane/water and lubricant oil/water systems. The experimental data follow a distribution similar to that discussed in the ***Section 3.2***, where a Rayleigh distribution reasonably fits the data. The technique is also suitable to rank emulsion stability, as can be inferred from the two distinct distributions observed; in other words, coalescence is a random process and the experimental data show a remarkable dispersion, but a significant number of experiments allows one to estimate the probability of coalescence, which is an intrinsic property of the system.

As is the case with foams, the interferometric images enable the thin film thickness reconstruction. At the cost of a relatively manual process, it is possible to calculate the topography of the film and its evolution with time. Fig. 10b shows the mean film thickness versus time for the same two systems as in Fig. 10a. In both cases, $t = 0$ is given by the instant in which the stage controlling the drop vertical position stops moving, and the maximum thickness that can be measured is optically limited ($\sim 1\,\mu$m). It is worth mentioning that, in these experiments, no dimple was observed, which does not necessarily mean that a dimple was not formed during the initial stages where $h > 1\,\mu$m. As can be seen in Fig. 10b, the mean film thickness reasonably follows a power law of the form $\bar{h}(t) \propto t^{-\xi}$, where the best fit values for $-\xi$ (-1.03 and -0.68 for the silicone oil and the squalane, respectively) interestingly coincide with those expected respectively for a plug flow and poiseuille flow inside the thin film [215].

5.2.2. Drop rupture dynamics and retraction speed

The experimental setup represented in Fig. 1c is also an excellent platform to study the hole nucleation mentioned in ***Section 5.1***. The substitution of the side camera by a high speed camera allows one to track the growth of the hole, as shown in Fig. 11. The retraction of the thin film during coalescence is a rich phenomenon that has been studied over decades [216], with an increased interest after the development of digital high speed cameras opened the door towards its direct visualization. There exist different regimes, where the Ohnesorge number, defined as,

$$Oh = \frac{\mu}{\sqrt{\rho \sigma_{\alpha\beta} h_r}}, \tag{32}$$

tells us whether the system pertains to the inertial regime ($Oh \ll 1$) or the viscous regime ($Oh > 1$) [216]. Here μ is the dynamic viscosity of the continuous phase, ρ is the density of the continuous phase, $\sigma_{\alpha\beta}$ is the surface tension, and h_r is the film thickness at rupture.

In the examination of the inertial regime, several research

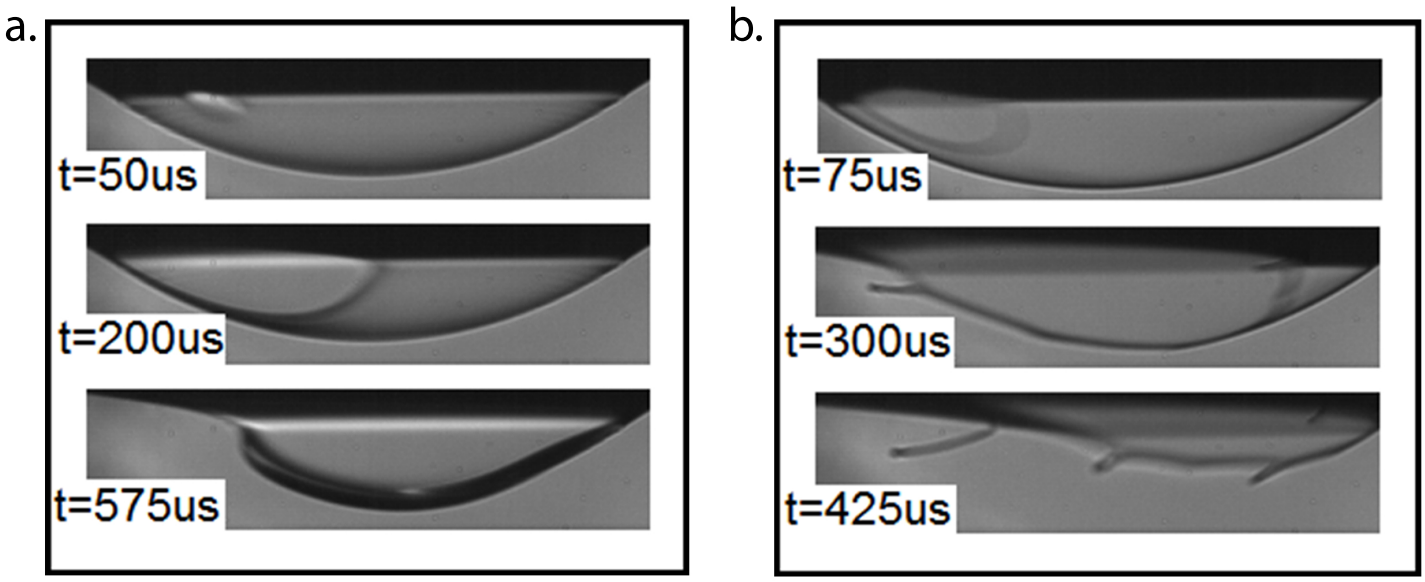

Figure 11: Snapshots of the film rupture acquired by means of a high speed camera used as the side camera in Fig. 1. In both cases, the lower and upper phases are DI water, and the thin film is a 50 cSt pure silicone oil. Two distinct regimes are observed. In the left images (**a.**), the film ruptured at a much larger thickness than that corresponding to the right images (**b.**), so that $Oh_{\text{right}} \gg Oh_{\text{left}}$. A rim is clearly observed in the left images, growing in size as the film retracts and fluid volume accumulates. On the contrary, tendrils of oil are left behind on the hole perimeter in the right images, where the Oh number is lower.

efforts have found an increase of the radius of the hole following $r \sim \sqrt{t}$ [217–222], with the mass of the retracting film accumulating in a torus-shaped rim. For $Oh \gtrsim 1$, a model was proposed where the radius of the hole follows $r/R \sim t/t_v(\ln(t/t_v))$, being R the drop radius and t_v the viscous time defined as [223],

$$t_v = \frac{R\mu}{\sigma_{\alpha\beta}}. \tag{33}$$

Later experiments found a relationship $r \sim t$ for this regime [218, 220, 221] and, very recently, Zhang *et al.* [224] have used a single drop setup to confirm the above-mentioned $r \sim \sqrt{t}$ and $r \sim t$ relationships for the inertial and viscous regimes, respectively. Aryafar and Kavehpour [225] pointed out a possible explanation for the observed discrepancy in the high Oh regime: the rim of the hole becomes unstable, forming tendrils that eventually produce micron sized droplets. Since the hole radius is normally measured from side images (measuring the length of the neck between the two droplets or the droplet and the planar interface), this instability could not be observed in most of the experiments cited above.

Another instance in which the visualization of the neck (and not the hole) may not fully capture the complexity of the hole growth is the case of the two interfaces entrapping a thin film that has a different interfacial tension at either liquid-liquid interface due to, for example, a different aging process. Malmazet *et al.* [226] conducted coalescence experiments where a water droplet is released from a capillary immersed in oil. Once released, the droplet descends and reaches an oil/water interface, which has been aged and shows a lower interfacial tension. When coalescence happens, they observed the rim bending towards the inside of the drop, i.e., towards the interface showing a higher interfacial tension.

Images of a torus-shaped rim and an unstable rim with tendrils are shown in Fig. 11. Note that these images were obtained by means of the substitution of the side camera represented in Fig. 1c by a high speed camera. In other words, the setup can still simultaneously work as an interferometer, providing the topography of the film when coalescence takes place. Since the film thickness is of critical importance to the mechanism leading to the observed instability at high Oh numbers [216], the single drop setup is a promising tool to further analyze this phenomenon.

6. Conclusion and Outlook

Single bubble/drop techniques have improved our understanding of foam and emulsion physics by providing insights that complement those obtained from the bulk foam/emulsion and single film tests. Typical bubble/drop setups contain an arrangement to form bubbles/drops of

controlled volume (often supported on a capillary), cameras to visualize the shape of the bubble/drop, pressure transducers to monitor the internal pressure, and an arrangement (usually based on interferometry) to measure the spatiotemporal film thickness evolution between the interacting interfaces of bubbles or drops. Major measurables from single bubble/drop experiments include coalescence times and their distributions, the spatiotemporal film profiles both during drainage (utilizing thin film interferometry) and rupture (utilizing a high speed imaging camera), and interfacial rheology.

Single bubble/drop techniques will continue to be an important tool for studying foams and emulsions. Future work in this area can be split into two categories. Firstly, efforts can be aimed at improving the single bubble/drop setups and the associated protocols. These include (a) improving film thickness measurement tools (interferometry or otherwise) for studying emulsions with low refractive indices (eg. flurosilicone-water emulsions), (b) improving the robustness and spatiotemporal resolution of automated film thickness measurement tools (eg. for interferometry), (c) developing a generalized theory for describing coalescence time distributions across bubbles, anti-bubbles, and drops, and (d) investigating the role of bubble size (super or sub hemispherical cap) on the accuracy of dilatational rheology measurements. Secondly, efforts can be aimed at utilizing single bubble/drop setups to resolve unanswered questions in foam and emulsion physics. These include (a) investigating antifoam mechanics in non-aqueous systems, (b) characterizing evaporation driven solutocapillary bubble destabilization, and (c) investigating the effects of interfacial rheology on the dynamics of bubble rupture.

Acknowledgements

We thank John Frostad and Simone Bochner de Araujo for constructing the experimental setups reported in this manuscript, and Prem Sai for the schematic illustrations in the manuscript. This study was partially supported by grants from Shell and the Beijing Welltrailing Science and Technology Company.

Appendix A. Matlab Codes

The MATLAB® codes for computing the coalescence time distributions can be obtained at

1. Coalescence time curves - https://github.com/vcsuja/Coalescence-Time-Distributions
2. Color Map generator - https://github.com/vcsuja/ColorMapGenerator

Appendix B. Simple Emulsion/Foam Model

Here we will provide more details about obtaining equation 5 reported in the manuscript.

Multiplying eq. 3 in the manuscript by $d(t)$ and substituting eq. 4 in the manuscript we obtain:

$$\frac{dN(t)}{dt}d(t) = -3fN(t)d^3(t) = -3fk.$$

Eliminating $d(t)$ and integrating we obtain the following,

$$\begin{aligned}\sqrt[3]{\frac{k}{N(t)}}dN &= -3fk\,dt,\\ \int_0^t \frac{dN}{\sqrt[3]{N(t)}} &= -3fk^{2/3}\int_0^t dt,\\ N(t)^{2/3} &= -2fk^{2/3} + C.\end{aligned}$$

Utilizing the initial condition $N(t=0) = k/d_0^3$ and simplifying we obtain eq. 5 in the manuscript.

$$\frac{1}{d_0^2} - \frac{1}{d^2(t)} = 2ft.$$

Appendix C. Cumulative Coalescence Time Distributions

Weibull distribution

The Weibull distribution is a two parameter continuous probability distribution for positive valued random variables.

The probability density function of the Weibull distribution is given by,

$$p_w(t;\lambda,k) = \begin{cases} \frac{k}{\lambda}\left(\frac{t}{\lambda}\right)^{k-1} e^{-(t/\lambda)^k} & t \geq 0,\\ 0 & t < 0,\end{cases}$$

Here t is the time, λ is the scale parameter and k is the shape parameter of the distribution. Thus, physically $p_w(t;\lambda;k)$ gives the probability of observing a coalescence event at time t.

The corresponding cumulative distribution function (CDF) used for determining the cumulative coalescence time curves is given by,

$$P_w(t;\lambda,k) = 1 - e^{-(t/\lambda)^k}. \tag{C.1}$$

The maximum likelihood estimator for the scale and shape parameter are given by the following equations,

$$\hat{\lambda}^k = \frac{1}{n}\sum_{i=1}^{n} t_i^k$$

$$\frac{\sum_{i=1}^{n} t_i^{\hat{k}} \ln t_i}{\sum_{i=1}^{n} t_i^{\hat{k}}} - \frac{1}{\hat{k}} - \frac{1}{n}\sum_{i=1}^{n} t_i^{\hat{k}} = 0$$

The implicit equation for $\hat{k}$ is usually numerically solved, before solving for $\hat{\lambda}$ analytically.

Rayleigh distribution

The Rayleigh distribution is a continuous probability distribution for positive valued random variables and is known to adequately describe the experimentally observed distribution of bubble coalescence times [92, 99]. The Rayleigh distribution can be obtained by setting $\lambda = \sqrt{2}\sigma$ and $k = 2$ in the Weibull distribution. Hence, the probability density function of the Rayleigh distribution is given by,

$$p_r(t;\sigma) = \frac{t}{\sigma^2} e^{-t^2/(2\sigma^2)}, \qquad t \geq 0$$

Here t is the time and σ is the scale parameter of the distribution. Thus, physically $p_r(t;\sigma)$ gives the probability of observing a coalescence event at time t.

The corresponding cumulative distribution function (CDF) used for determining the cumulative coalescence time curves is given by,

$$P_r(t;\sigma) = \int_0^x p(t;\sigma) = 1 - e^{-t^2/(2\sigma^2)}$$

The Expectation-Maximization algorithm

In the presence of antifoam particles, the distribution of bubble coalescence times are best described by a mixture of n distributions. In such cases the complete CDF is given by,

$$P_m(t;\lambda_1,\lambda_2...\lambda_n;k_1,k_2...k_n) = \sum_{i=1}^{n} x_i P(t;\lambda_i;k_i), \qquad \sum_{i=1}^{N} x_i = 1$$

To determine the unknown mixture ratios (x_i) the scale parameters (λ_i) and the shape parameter (k_i) where applicable, we utilize the Expectation-Maximization algorithm [102]. The Expectation-Maximization algorithm is an iterative algorithm that performs the following:

1. Expectation step: Given n distributions (with some scale parameters, shape parameters and mixtures ratios), the algorithm calculates the likelihood that a given point in the data set was drawn from a particular (say a Rayleigh) distribution.
2. Maximization step: Given the data-distribution association likelihoods, the algorithm re-calculates the conditional (Bayesian) likelihoods, which is then used to re-calculate the scale and mixture ratios. This procedure is repeated till the scale and mixture ratios converge. A Matlab implementation of this algorithm for Weibull, Rayleigh and Villermaux distributions utilized in this paper is available in github (see manuscript for the weblinks).

Best fit Parameters

The best fit scale and shape (where applicable) parameters for the cummulative coalescence time distributions shown in Fig.3 are reported in Tables C.1 - C.4

Appendix D. Intensity of light reflected from a thin film

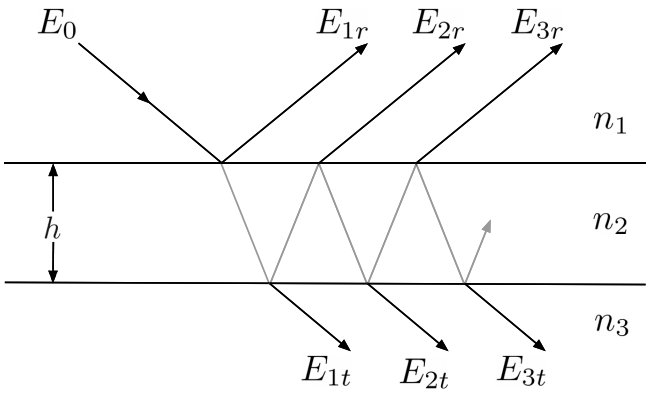

Figure D.12: A schematic showing light reflecting and refracting upon a non-absorbing thin film. The film has a thickness d and refractive index n_2, and is bound on either sides by media having refractive index of n_1 and n_3.

Here we will develop the intensity relation for the light reflected of a thin film. The following assumptions are made:

1. The film is non-dispersive i.e all wavelengths have the same refractive index.
2. The film is non-absorbing i.e the film does not attenuate the light intensity.
3. The angle of incidence is low i.e the polarization of the light does not matter and Fresnel reflection and transmission coefficients do not depend on the incidence angle.

Distribution	Scale parameter	Shape Parameter	Kolmogrov-Smirov p-value	R^2
Weibull	6.27	1.49	0.991	1
Rayleigh	4.91	N/A	0.433	0.992
Villermaux	6.06	N/A	1	1

Table C.1: The parameters of the different distributions for bubbles coalescing in deionized water from Villermaux et.al [94]

Distribution	Scale parameter	Shape Parameter	Kolmogrov-Smirov p-value	R^2
Weibull	112.48	4.92	1	0.979
Rayleigh	75.15	N/A	0.1433	0.851
Villermaux	104.3	N/A	0.019	0.801

Table C.2: The parameters of the different distributions for antibubbles coalescing in a mixture water with 10% glycerol from Vermant et.al [93]

Distribution	Scale parameter	Shape Parameter	Kolmogrov-Smirov p-value	R^2
Weibull	853.90	2.977	0.771	0.922
Rayleigh	572.09	N/A	0.275	0.874
Villermaux	779.98	N/A	0.135	0.825

Table C.3: The parameters of the different distributions for silicone oil drops coalescing in an aqueous polymer solution from Milad et.al [24]

Distribution	Scale parameter with antifoam	Shape Parameter with antifoam	Scale parameter w/o antifoam	Shape Parameter w/o antifoam	Kolmogrov-Smirov p-value	R^2
Weibull	95.9	5.96	2806.1	2.153	0.9748	0.916
Rayleigh	63.8	N/A	1955.6	N/A	0.975	0.918
Villermaux	88.6	N/A	2526.2	N/A	0.975	0.930

Table C.4: The parameters of the different distributions for bubbles coalescing in lubricants with antifoams from Suja et.al [9]

Following Hecht[124], in complex representation, we have the following expression of reflected electric field,

$$\begin{aligned}
\tilde{E}_{1r} &= E_0 r_{12} e^{i\omega t} \\
\tilde{E}_{2r} &= E_0 t_{12} r_{23} t_{21} e^{i(\omega t - \delta)} \\
\tilde{E}_{3r} &= E_0 t_{12} r_{23}^2 r_{21} t_{21} e^{i(\omega t - 2\delta)} \\
&\vdots \\
\tilde{E}_{Nr} &= E_0 t_{12} r_{23}^{N-1} r_{21}^{N-2} t_{21} e^{i[\omega t - (N-1)\delta]}
\end{aligned}$$

Here, $E_0 e^{i\omega t}$ is the incident wave, ω is frequency and $\delta = 4\pi n_2 h/\lambda$ is the phase difference. r and t are the Fresnel reflection and transmission amplitude coefficients given by,

$$\begin{aligned}
r_{12} = -r_{21} &= \frac{n_1 - n_2}{n_1 + n_2} \\
r_{23} = -r_{32} &= \frac{n_2 - n_3}{n_2 + n_3} \\
t_{12} = -t_{21} &= 1 - r_{12} \\
t_{23} = -t_{32} &= 1 - r_{23}
\end{aligned}$$

Similarly, the transmitted electric field is given by,

$$\begin{aligned}
\tilde{E}_{1t} &= E_0 t_{12} t_{23} e^{i\omega t} \\
\tilde{E}_{2t} &= E_0 t_{12} r_{23} r_{21} t_{23} e^{i(\omega t - \delta)} \\
\tilde{E}_{3t} &= E_0 t_{12} (r_{23} r_{21})^2 t_{23} e^{i(\omega t - 2\delta)} \\
&\vdots \\
\tilde{E}_{Nt} &= E_0 t_{12} (r_{23} r_{21})^{N-1} t_{23} e^{i[\omega t - (N-1)\delta]}
\end{aligned}$$

Two reflections

If we only consider the first two reflections, we obtain the following expressions for the intensity,

$$\tilde{E}_r = E_0 e^{i\omega t} \left(r_{12} + t_{12} r_{23} t_{21} e^{-i\delta} \right)$$

The reflected light intensity, $I_r = E_r E_r^*/2$ is obtained after algebra as,

$$I_r = I_0 \left(r_{12}^2 + r_{12} r_{23} (1 - r_{12}^2) \cos\delta + r_{23}^2 (1 - r_{12}^2)^2 \right)$$

Here E_r^* is the complex conjugate of E_r.
Replacing the Fresnel amplitude coefficients by the power coefficients we obtain the following expression,

$$\begin{aligned}
I(\lambda, d) = I_0(\lambda) \big(& R_1 + R_2 (1 - R_1)^2 \\
& + 2\sqrt{R_1 R_2 (1 - R_1)^2} \cos(\phi) \big) \qquad \text{(D.1)} \\
\phi = \frac{4\pi n_2 h}{\lambda} & + \pi(\mathbb{1}(n_2 > n_1)) + \pi(\mathbb{1}(n_3 > n_2)) \qquad \text{(D.2)}
\end{aligned}$$

Here,

$$\begin{aligned}
R_1 = (r_{12})^2 = (-r_{21})^2 &= \left(\frac{n_1 - n_2}{n_1 + n_2} \right)^2 \\
R_2 = (r_{23})^2 = (-r_{32})^2 &= \left(\frac{n_2 - n_3}{n_2 + n_3} \right)^2
\end{aligned}$$

Note that the additional terms inside the phase difference selects the right sign among the dual roots of $\sqrt{R_1 R_2}$.

Infinite reflections

To treat this limit, it is easier to calculate the transmitted light intensity and then obtain the reflected light intensity as the complement. This is possible due to assumption 2.
Summing up the terms in the transmitted electric field, we obtain

$$\tilde{E}_t = E_0 e^{i\omega t} t_{12} t_{23} \left(1 + r_{23} r_{21} e^{-i\delta} + (r_{23} r_{21})^2 e^{-2i\delta} + \ldots \right)$$

The above geometric series converges to,

$$\tilde{E}_t = E_0 e^{i\omega t} \left[\frac{t_{12} t_{23}}{1 - r_{23} r_{21} e^{-i\delta}} \right]$$

The transmitted light intensity, $I_t = E_t E_t^*/2$ is obtained after algebra as,

$$\frac{I_t}{I_0} = \frac{(1 - r_{12}^2)(1 - r_{23}^2)}{1 + (r_{23} r_{21})^2 - 2 r_{23} r_{21} \cos\delta}$$

To be consistent with literature [38], we will use the following trigonometric identity, $\cos\delta = 1 - 2\sin^2\beta$. Here $\delta = 2\beta$. Applying this identity, rearranging and taking the complement, we obtain

$$\frac{I_r}{I_0} = 1 - \frac{(1 - r_{12}^2)(1 - r_{23}^2)}{(1 - r_{23} r_{21})^2 + 4 r_{23} r_{21} \sin^2\beta}$$

Introducing,

$$\Delta = \frac{I - I_{min}}{I_{max} - I_{min}}$$

We have the following expression,

$$\sin^2\beta = \frac{\Delta}{1 + \frac{4 r_{23} r_{21}}{(1 - r_{23} r_{21})^2} (1 - \Delta)}$$

Expressing β in the above equation in terms of h, we obtain Eq.13 from which the thickness of the film can be calculated.

References

[1] Frostad JM, Paul A, Leal LG. Coalescence of droplets due to a constant force interaction in a quiescent viscous fluid. Physical Review Fluids. 2016;1(3):033904.

[2] Pugh RJ. Bubble and foam chemistry. Cambridge University Press; 2016.

[3] Garrett PR. The science of defoaming: theory, experiment and applications. vol. 155. CRC Press; 2016.

[4] Patino JMR, Sanchez CC, Niño MRR. Implications of interfacial characteristics of food foaming agents in foam formulations. Advances in Colloid and Interface Science. 2008;140(2):95–113.

[5] Qian S, Wu Z, Zheng H, Geng Y. Study on riboflavin recovery from wastewater by a batch foam separation process. Separation Science and Technology. 2009;44(11):2681–2694.

[6] Evans DE, Sheehan MC. Don't be fobbed off: The substance of beer foam—A review. Journal of the American Society of Brewing Chemists. 2002;60(2):47–57.

[7] Kitchener J. The froth flotation process: past, present and future-in brief. In: The Scientific Basis of Flotation. Springer; 1984. p. 3–51.

[8] Suja VC, Kar A, Cates W, Remmert S, Savage P, Fuller G. Evaporation-induced foam stabilization in lubricating oils. Proceedings of the National Academy of Sciences. 2018;115(31):7919–7924.

[9] Suja VC, Kar A, Cates W, Remmert S, Fuller G. Foam stability

in filtered lubricants containing antifoams. Journal of Colloid and Interface Science. 2020;567:1–9.
[10] Sawicki GC. High-Performance Antifoams for the Textile Dyeing Industry. In: Surfactant Sci. Ser.. vol. 45. Marcel Dekker New York; 1992. p. 193.
[11] Tsang YF, Chua H, Sin S, Tam C. A novel technology for bulking control in biological wastewater treatment plant for pulp and paper making industry. Biochemical Engineering Journal. 2006;32(3):127–134.
[12] Leal-Calderon F, Schmitt V, Bibette J. Emulsion science: basic principles. Springer Science & Business Media; 2007.
[13] Chappat M. Some applications of emulsions. Colloids and Surfaces A: Physicochemical and Engineering Aspects. 1994;91:57–77.
[14] Mandal A, Samanta A, Bera A, Ojha K. Characterization of oil-water emulsion and its use in enhanced oil recovery. Industrial & Engineering Chemistry Research. 2010;49(24):12756–12761.
[15] Tadros TF. Colloids in paints. vol. 6. John Wiley & Sons; 2011.
[16] Harika E, Helene M, Bouyer J, Fillon M. Impact of lubricant contamination with water on hydrodynamic thrust bearing performance. Mécanique & industries. 2011;12(5):353–359.
[17] Bochner de Araujo S, Merola M, Vlassopoulos D, Fuller GG. Droplet coalescence and spontaneous emulsification in the presence of asphaltene adsorption. Langmuir. 2017;33(40):10501–10510.
[18] Azim AAAA, Abdul-Raheim ARM, Kamel RK, Abdel-Raouf ME. Demulsifier systems applied to breakdown petroleum sludge. Journal of Petroleum Science and Engineering. 2011;78(2):364–370.
[19] Umar AA, Saaid IBM, Sulaimon AA, Pilus RBM. A review of petroleum emulsions and recent progress on water-in-crude oil emulsions stabilized by natural surfactants and solids. Journal of Petroleum Science and Engineering. 2018;165:673–690.
[20] D892-13 A. Standard Test Method for Foaming Characteristics of Lubricating Oils. ASTM International West Conshohocken, PA; 2013.
[21] Denkov ND. Mechanisms of foam destruction by oil-based antifoams. Langmuir. 2004;20(22):9463–9505.
[22] ISO 12152:2012-08. Lubricants, Industrial Oils and Related Products – Determination of the Foaming and Air Release Properties of Industrial Gear Oils Using a Spur Gear Test Rig/ Flender Foam Test Procedure. Geneva, CH: International Organization for Standardization; 2012.
[23] D1401-19 A. Standard Test Method for Water Separability of Petroleum Oils and Synthetic Fluids. ASTM International West Conshohocken, PA; 2019.
[24] Kamkar M, Bazazi P, Kannan A, Chandran Suja V, Hejazi SH, Fuller GG, et al. Polymeric-Nanofluids Stabilized Emulsions: Interfacial versus Bulk Rheology. Journal of Colloid and Interface Science. 2020;.
[25] Lobo L, Svereika A, Nair M. Coalescence during emulsification: 1. Method development. Journal of colloid and interface science. 2002;253(2):409–418.
[26] Joscelyne SM, Trägårdh G. Membrane emulsification—a literature review. Journal of Membrane Science. 2000;169(1):107–117.
[27] Vladisavljević GT, Schubert H. Influence of process parameters on droplet size distribution in SPG membrane emulsification and stability of prepared emulsion droplets. Journal of Membrane Science. 2003;225(1-2):15–23.
[28] Pugh R. Foaming, foam films, antifoaming and defoaming. Advances in Colloid and Interface Science. 1996;64:67–142.
[29] Friberg SE. Foams from non-aqueous systems. Current opinion in colloid & interface science. 2010;15(5):359–364.
[30] Pugh R. Experimental techniques for studying the structure of foams and froths. Advances in Colloid and Interface Science. 2005;114:239–251.
[31] Fameau AL, Saint-Jalmes A. Non-aqueous foams: Current understanding on the formation and stability mechanisms. Advances in colloid and interface science. 2017;247:454–464.
[32] Exerowa D, Kruglyakov PM. Foam and foam films: theory, experiment, application. Elsevier; 1997.
[33] Mcclements DJ. Critical review of techniques and methodologies for characterization of emulsion stability. Critical reviews in food science and nutrition. 2007;47(7):611–649.
[34] Miralles V, Selva B, Cantat I, Jullien MC. Foam drainage control using thermocapillary stress in a two-dimensional microchamber. Physical Review Letters. 2014;112(23):238302.
[35] Exerowa D, Gochev G, Platikanov D, Liggieri L, Miller R. Foam Films and Foams: Fundamentals and Applications. CRC Press; 2018.
[36] Scheludko A, Exerowa D. Device for interferometric determination of the thickness of microscopic foam films. Commun Dep Chem(Bulg Acad Sci). 1959;7:123.
[37] Mysels KJ. Soap Films and Some Problems in Surface and Colloid Chemistry1. The Journal of Physical Chemistry. 1964;68(12):3441–3448.
[38] Sheludko A. Thin liquid films. Advances in Colloid and Interface Science. 1967;1(4):391–464.
[39] Exerowa D, Gotchev G, Levecke B, Tadros T. Emulsion Newton black films stabilized by polymeric surfactants. CR Acad Bulgare Sci. 2008;61:455–468.
[40] Mysels KJ, Jones MN. Direct measurement of the variation of double-layer repulsion with distance. Discussions of the Faraday Society. 1966;42:42–50.
[41] Dippenaar A. The destabilization of froth by solids. I. The mechanism of film rupture. International Journal of Mineral Processing. 1982;9(1):1–14.
[42] Stubenrauch C, Von Klitzing R. Disjoining pressure in thin liquid foam and emulsion films—new concepts and perspectives. Journal of Physics: condensed matter. 2003;15(27):R1197.
[43] Joye JL, Hirasaki GJ, Miller CA. Asymmetric drainage in foam films. Langmuir. 1994;10(9):3174–3179.
[44] Langevin D. Bubble coalescence in pure liquids and in surfactant solutions. Current Opinion in Colloid & Interface Science. 2015;20(2):92–97.
[45] Chan DY, Klaseboer E, Manica R. Film drainage and coalescence between deformable drops and bubbles. Soft Matter. 2011;7(6):2235–2264.
[46] Kannan A, Shieh IC, Leiske DL, Fuller GG. Monoclonal antibody interfaces: dilatation mechanics and bubble coalescence. Langmuir. 2018;34(2):630–638.
[47] Kannan A, Shieh IC, Fuller GG. Linking aggregation and interfacial properties in monoclonal antibody-surfactant formulations. Journal of colloid and interface science. 2019;550:128–138.
[48] Gochev G, Platikanov D, Miller R. Chronicles of foam films. Advances in Colloid and Interface Science. 2016;233:115–125.
[49] Plateau J. Statique expérimentale et théorique des liquides soumis aux seules forces moléculaires. vol. 2. Gauthier-Villars; 1873.
[50] Isenberg C. Soap films and bubbles. Physics Education. 1981;16(4):218.
[51] Boys CV. Soap-Bubbles and the Forces which Mould Them. Society for Promoting Christian Knowledge; 1890.
[52] Worthington AM. II. On pendent drops. Proceedings of the Royal Society of London. 1881;32(212-215):362–377.
[53] Edgerton HE, Hauser EA, Tucker W. Studies in drop formation as revealed by the high-speed motion camera. Journal of Physical Chemistry. 1937;41(7):1017–1028.
[54] Berry JD, Neeson MJ, Dagastine RR, Chan DY, Tabor RF.

Measurement of surface and interfacial tension using pendant drop tensiometry. Journal of colloid and interface science. 2015;454:226–237.
[55] Simon M. Recherches sur la capillarité. In: Annales de Chimie et de Physique. vol. 32; 1851. p. 5.
[56] Mysels KJ. The maximum bubble pressure method of measuring surface tension, revisited. Colloids and surfaces. 1990;43(2):241–262.
[57] Schrödinger E. Notiz über den Kapillardruck in Gasblasen. Annalen der Physik. 1915;351(3):413–418.
[58] Fuller GG, Vermant J. Complex Fluid-Fluid Interfaces: Rheology and Structure. Annual Review of Chemical and Biomolecular Engineering. 2012;3(1):519–543.
[59] Marangoni C. The principle of the surface viscosity of liquids established by mr. j. plateau. NCim. 1972;5:239–273.
[60] Boussinesq J. Existence of a superficial viscosity in the thin transition layer separating one liquid from another contiguous fluid. CR Hehbd Seanc Acad Sci. 1913;156:983–989.
[61] Scriven L. Dynamics of a fluid interface equation of motion for Newtonian surface fluids. Chemical Engineering Science. 1960;12(2):98–108.
[62] Lunkenheimer K, Hartenstein C, Miller R, Wantke KD. Investigation on the method of the radially oscillating bubble. Colloids and surfaces. 1984;8(3):271–288.
[63] Nagarajan R, Wasan D. Measurement of dynamic interfacial tension by an expanding drop tensiometer. Journal of colloid and interface science. 1993;159(1):164–173.
[64] Rayleigh L. XX. On the equilibrium of liquid conducting masses charged with electricity. The London, Edinburgh, and Dublin Philosophical Magazine and Journal of Science. 1882;14(87):184–186.
[65] Clayton W. The theory of emulsions and emulsification. J. & A. Churchill; 1923.
[66] Wilson C, Taylor G; Cambridge University Press. The bursting of soap-bubbles in a uniform electric field. Mathematical proceedings of the Cambridge philosophical society. 1925;22(5):728–730.
[67] Dewar J. Soap bubbles of long duration. Journal of the Franklin Institute. 1919;188(6):713–749.
[68] Derjaguin B, Kussakov M. Anomalous properties of thin polymolecular films. Acta Physicochim URSS. 1939;10(1):25–44.
[69] Rehbinder P, Wenström E. Stabilisierende Wirkung von Adsorptionsschichten grenzflächenaktiver Stoffe auf disperse Systeme. II. Stabilität von Blasen und Tropfen an Trennungsflächen. Kolloid-Zeitschrift. 1930;53(2):145–158.
[70] Charles GE, Mason SG. The coalescence of liquid drops with flat liquid/liquid interfaces. Journal of Colloid Science. 1960;15(3):236–267.
[71] Frostad JM, Tammaro D, Santollani L, de Araujo SB, Fuller GG. Dynamic fluid-film interferometry as a predictor of bulk foam properties. Soft matter. 2016;12(46):9266–9279.
[72] Chandran Suja V, Frostad J, Fuller G. Impact of compressibility on the control of bubble-pressure tensiometers. Langmuir. 2016;32(46):12031–12038.
[73] Chandran Suja V, Hadidi A, Kannan A, Fuller GG. Symmetry breaking and chaos in evaporation driven Marangoni flows over bubbles. arXiv preprint arXiv:200409752. 2020;.
[74] Chandran Suja V, Kannan A, Kubicka BA, Hadidi A, Fuller GG. Bubble coalescence at wormlike micellar solution-air interfaces. Langmuir. 2020;.
[75] Allan RS, Charles G, Mason S. The approach of gas bubbles to a gas/liquid interface. Journal of Colloid Science. 1961;16(2):150–165.
[76] Zhang F, Thoraval MJ, Thoroddsen ST, Taborek P. Partial coalescence from bubbles to drops. Journal of Fluid Mechanics. 2015;782:209–239.
[77] Feng J, Muradoglu M, Kim H, Ault JT, Stone HA. Dynamics of a bubble bouncing at a liquid/liquid/gas interface. Journal of Fluid Mechanics. 2016;807:324–352.
[78] Krzan M, Lunkenheimer K, Malysa K. Pulsation and bouncing of a bubble prior to rupture and/or foam film formation. Langmuir. 2003;19(17):6586–6589.
[79] Menesses M, Roché M, Royon L, Bird JC. Surfactant-free persistence of surface bubbles in a volatile liquid. Physical Review Fluids. 2019;4(10):100506.
[80] Suñol F, González-Cinca R. Rise, bouncing and coalescence of bubbles impacting at a free surface. Colloids and Surfaces A: Physicochemical and Engineering Aspects. 2010;365(1-3):36–42.
[81] Sett S, Sinha-Ray S, Yarin A. Gravitational drainage of foam films. Langmuir. 2013;29(16):4934–4947.
[82] Paulsen JD, Carmigniani R, Kannan A, Burton JC, Nagel SR. Coalescence of bubbles and drops in an outer fluid. Nature communications. 2014;5(1):1–7.
[83] Bluteau L, Bourrel M, Passade-Boupat N, Talini L, Verneuil E, Lequeux F. Water film squeezed between oil and solid: drainage towards stabilization by disjoining pressure. Soft matter. 2017;13(7):1384–1395.
[84] Blanchette F, Bigioni TP. Partial coalescence of drops at liquid interfaces. Nature Physics. 2006;2(4):254–257.
[85] MacKay G, Mason S. The gravity approach and coalescence of fluid drops at liquid interfaces. The Canadian Journal of Chemical Engineering. 1963;41(5):203–212.
[86] Gillespie T, Rideal EK. The coalescence of drops at an oil-water interface. Transactions of the Faraday Society. 1956;52:173–183.
[87] Basheva ES, Gurkov TD, Ivanov IB, Bantchev GB, Campbell B, Borwankar RP. Size dependence of the stability of emulsion drops pressed against a large interface. Langmuir. 1999;15(20):6764–6769.
[88] Politova NI, Tcholakova S, Tsibranska S, Denkov ND, Muelheims K. Coalescence stability of water-in-oil drops: Effects of drop size and surfactant concentration. Colloids and Surfaces A: Physicochemical and Engineering Aspects. 2017;531:32–39.
[89] Aarts DG, Lekkerkerker HN. Droplet coalescence: drainage, film rupture and neck growth in ultralow interfacial tension systems. Journal of fluid mechanics. 2008;606:275–294.
[90] Klaseboer E, Chevaillier JP, Gourdon C, Masbernat O. Film drainage between colliding drops at constant approach velocity: experiments and modeling. Journal of colloid and interface science. 2000;229(1):274–285.
[91] Vakarelski IU, Manica R, Tang X, O'Shea SJ, Stevens GW, Grieser F, et al. Dynamic interactions between microbubbles in water. Proceedings of the National Academy of Sciences. 2010;107(25):11177–11182.
[92] Zheng Q, Klemas V, Hsu YH. Laboratory measurement of water surface bubble life time. Journal of Geophysical Research: Oceans. 1983;88(C1):701–706.
[93] Vitry Y, Dorbolo S, Vermant J, Scheid B. Controlling the lifetime of antibubbles. Advances in colloid and interface science. 2019;.
[94] Poulain S, Villermaux E, Bourouiba L. Ageing and burst of surface bubbles. Journal of Fluid Mechanics. 2018;851:636–671.
[95] Kabalnov AS. Chapter 7 - Coalescence in Emulsions. In: Modern Aspects of Emulsion Science. The Royal Society of Chemistry; 1998. p. 205–260.
[96] Deminiere B, Colin A, Leal-Calderon F, Muzy JF, Bibette J. Cell Growth in a 3D Cellular System Undergoing Coalescence. Phys Rev Lett. 1999 Jan;82:229–232.
[97] Tobin S, Meagher A, Bulfin B, Möbius M, Hutzler S. A public study of the lifetime distribution of soap films. American Journal of Physics. 2011;79(8):819–824.

[98] Ghosh P. Coalescence of air bubbles at air–water interface. Chemical Engineering Research and Design. 2004;82(7):849–854.
[99] Lhuissier H, Villermaux E. Bursting bubble aerosols. Journal of Fluid Mechanics. 2012;696:5–44.
[100] Ghosh P, Juvekar V. Analysis of the drop rest phenomenon. Chemical Engineering Research and Design. 2002;80(7):715–728.
[101] Sornette D. Critical phenomena in natural sciences: chaos, fractals, selforganization and disorder: concepts and tools. Springer Science & Business Media; 2006.
[102] Moon TK. The expectation-maximization algorithm. IEEE Signal processing magazine. 1996;13(6):47–60.
[103] Bhamla MS, Chai C, Rabiah NI, Frostad JM, Fuller GG. Instability and breakup of model tear films. Investigative ophthalmology & visual science. 2016;57(3):949–958.
[104] Hermans E, Bhamla MS, Kao P, Fuller GG, Vermant J. Lung surfactants and different contributions to thin film stability. Soft matter. 2015;11(41):8048–8057.
[105] Shukla R, Udupa D, Das N, Mantravadi MV. Non-destructive thickness measurement of dichromated gelatin films deposited on glass plates. Optics & Laser Technology. 2006;38(7):552–557.
[106] Greco V, Lemmi C, Ledesma S, Molesini G, Puccioni G, Quercioli F. Measuring soap black films by phase shifting interferometry. Measurement Science and Technology. 1994;5(8):900.
[107] Habibi Y, Foulon L, Aguié-Béghin V, Molinari M, Douillard R. Langmuir–Blodgett films of cellulose nanocrystals: Preparation and characterization. Journal of Colloid and Interface Science. 2007;316(2):388–397.
[108] Zhang Y, Sharma V. Domain expansion dynamics in stratifying foam films: experiments. Soft matter. 2015;11(22):4408–4417.
[109] Zhang Y, Yilixiati S, Pearsall C, Sharma V. Nanoscopic terraces, mesas, and ridges in freely standing thin films sculpted by supramolecular oscillatory surface forces. ACS nano. 2016;10(4):4678–4683.
[110] Lv W, Zhou H, Lou C, Zhu J. Spatial and temporal film thickness measurement of a soap bubble based on large lateral shearing displacement interferometry. Applied optics. 2012;51(36):8863–8872.
[111] Vannoni M, Sordini A, Gabrieli R, Melozzi M, Molesini G. Measuring the thickness of soap bubbles with phase-shift interferometry. Optics express. 2013;21(17):19657–19667.
[112] Beltramo PJ, Vermant J. Simple Optical Imaging of Nanoscale Features in Free-Standing Films. ACS omega. 2016;1(3):363–370.
[113] Beltramo PJ, Van Hooghten R, Vermant J. Millimeter-area, free standing, phospholipid bilayers. Soft Matter. 2016;12(19):4324–4331.
[114] Kralchevsky P, Nikolov A, Wasan D, Ivanov I. Interaction of colloid particles in thinning foam films. Formation and expansion of dark spots. Langmuir. 1990;6:1180.
[115] Nikolov A, Wasan D. Ordered micelle structuring in thin films formed from anionic surfactant solutions. I. Experimental. J Colloid Interface Sci. 1989;133(1):1–12.
[116] Hendrix MH, Manica R, Klaseboer E, Chan DY, Ohl CD. Spatiotemporal evolution of thin liquid films during impact of water bubbles on glass on a micrometer to nanometer scale. Physical review letters. 2012;108(24):247803.
[117] Czakaj A, Kannan A, Wiśniewska A, Grześ G, Krzan M, Warszyński P, et al. Viscoelastic interfaces comprising of cellulose nanocrystals and lauroyl ethyl arginate for enhanced foam stability. Soft Matter. 2020;.
[118] Rodríguez-Hakim M, Barakat JM, Shi X, Shaqfeh ES, Fuller GG. Evaporation-driven solutocapillary flow of thin liquid films over curved substrates. Physical Review Fluids. 2019;4(3):034002.
[119] Rabiah NI, Scales CW, Fuller GG. The influence of protein deposition on contact lens tear film stability. Colloids and Surfaces B: Biointerfaces. 2019;180:229–236.
[120] Nierstrasz VA, Frens G. Marginal regeneration and the Marangoni effect. Journal of colloid and interface science. 1999;215(1):28–35.
[121] Lee J, Nikolov A, Wasan D. Surfactant micelles containing solubilized oil decrease foam film thickness stability. Journal of colloid and interface science. 2014;415:18–25.
[122] Rabiah NI, Sato Y, Kannan A, Kress W, Straube F, Fuller GG. Understanding the adsorption and potential tear film stability properties of recombinant human lubricin and bovine submaxillary mucins in an in vitro tear film model. Colloids and Surfaces B: Biointerfaces. 2020;p. 111257.
[123] Kitagawa K. Thin-film thickness profile measurement by three-wavelength interference color analysis. Applied optics. 2013;52(10):1998–2007.
[124] Hecht E. Optics. Pearson Education, Incorporated; 2017.
[125] Karakashev SI, Manev ED, Tsekov R, Nguyen AV. Effect of ionic surfactants on drainage and equilibrium thickness of emulsion films. Journal of colloid and interface science. 2008;318(2):358–364.
[126] Dong T, Weheliye WH, Angeli P. Laser induced fluorescence studies on the distribution of surfactants during drop/interface coalescence. Physics of Fluids. 2019;31(1):012106.
[127] Bordoloi AD, Longmire EK. Effect of neighboring perturbations on drop coalescence at an interface. Physics of Fluids. 2012;24(6):062106.
[128] Suja VC, Sentmanat J, Hofmann G, Scales C, Fuller GG. Hyperspectral imaging for dynamic thin film interferometry. Scientific reports. 2020;10(1):11378.
[129] Mandracchia B, Wang Z, Ferraro V, Villone MM, Di Maio E, Maffettone PL, et al. Quantitative imaging of the complexity in liquid bubbles' evolution reveals the dynamics of film retraction. Light: Science & Applications. 2019;8(1):1–12.
[130] Lin GL, Pathak JA, Kim DH, Carlson M, Riguero V, Kim YJ, et al. Interfacial dilatational deformation accelerates particle formation in monoclonal antibody solutions. Soft Matter. 2016;12(14):3293–3302.
[131] Lin G, Frostad JM, Fuller GG. Influence of interfacial elasticity on liquid entrainment in thin foam films. Physical Review Fluids. 2018;3(11):114001.
[132] Kannan A, Hristov P, Li J, Zawala J, Gao P, Fuller GG. Surfactant-laden bubble dynamics under porous polymer films. Journal of Colloid and Interface Science. 2020;.
[133] Rodríguez-Hakim M, Anand S, Tajuelo J, Yao Z, Kannan A, Fuller GG. Asphaltene-induced spontaneous emulsification: Effects of interfacial co-adsorption and viscoelasticity. Journal of Rheology. 2020;64(4):799–816.
[134] Nagel M, Tervoort TA, Vermant J. From drop-shape analysis to stress-fitting elastometry. Advances in colloid and interface science. 2017;247:33–51.
[135] Jaensson N, Vermant J. Tensiometry and rheology of complex interfaces. Current Opinion in Colloid & Interface Science. 2018;.
[136] Kotula AP, Anna SL. Regular perturbation analysis of small amplitude oscillatory dilatation of an interface in a capillary pressure tensiometer. Journal of Rheology. 2015;59(1):85–117.
[137] Wilde P, Mackie A, Husband F, Gunning P, Morris V. Proteins and emulsifiers at liquid interfaces. Advances in Colloid and Interface Science. 2004;108-109:63 – 71. Emulsions, From Fundamentals to Practical Applications.
[138] Fruhner H, Wantke KD, Lunkenheimer K. Relationship between surface dilational properties and foam stability. Col-

loids and Surfaces A: Physicochemical and Engineering Aspects. 2000;162(1-3):193–202.
[139] Sánchez-Puga P, Tajuelo J, Pastor J, Rubio M. Dynamic Measurements with the Bicone Interfacial Shear Rheometer: Numerical Bench-Marking of Flow Field-Based Data Processing. Colloids and Interfaces. 2018 Dec;2(4):69.
[140] Carvajal D, Laprade EJ, Henderson KJ, Shull KR. Mechanics of pendant drops and axisymmetric membranes. Soft Matter. 2011;7:10508–10519.
[141] Danov KD, Stanimirova RD, Kralchevsky PA, Marinova KG, Alexandrov NA, Stoyanov SD, et al. Capillary meniscus dynamometry - A method for determining the surface tension of drops and bubbles with isotropic and anisotropic surface stress distributions. Journal of Colloid and Interface Science. 2015;440:168 – 178.
[142] Leal LG. Advanced transport phenomena: fluid mechanics and convective transport processes. Cambridge University Press; 2007.
[143] Berg JC. An Introduction to Interfaces and Colloids: The Bridge to Nanoscience. World Scientific Publishing Co.; 2012.
[144] Murphy CL. Thermodynamics of low tension and highly curved interfaces [Ph.D. thesis]. University of Minnesota; 1966.
[145] Leermakers FAM, Barneveld PA, Sprakel J, Besseling NAM. Symmetric Liquid-Liquid Interface with a Nonzero Spontaneous Curvature. Phys Rev Lett. 2006;97(066103):1–4.
[146] Evans E, Yeung A. Hidden dynamics in rapid changes of bilayer shape. Chem Phys Lipids. 1994;73:39–56.
[147] Helfrich W. Elastic Properties of Lipid Bilayers: Theory and Possible Experiments. Z Naturforsch. 1973;28c:693–703.
[148] Zhong-can OY, Helfrich W. Bending energy of vesicle membranes: General expressions for the first, second, and third variation of the shape energy and applications to spheres and cylinders. Phys Rev A. 1989;39(10):5280–5288.
[149] Guckenberger A, Gekle s. Theory and algorithms to compute Helfrich bending forces: a review. J Phys: Condens Matter. 2017;29:203001.
[150] Lopez J, Hirsa A. Direct determination of the dependence of the surface shear and dilatational viscosities on the thermodynamic state of the interface: Theoretical foundations. Journal of colloid and interface science. 1998;206(1):231–239.
[151] Pepicelli M, Verwijlen T, Tervoort TA, Vermant J. Characterization and modelling of Langmuir interfaces with finite elasticity. Soft Matter. 2017;13:5977–5990.
[152] Petit P, Le Merrer M, Biance AL. Holes and cracks in rigid foam films. Journal of Fluid Mechanics. 2015;774.
[153] Rotenberg Y, Boruvka L, Neumann A. Determination of surface tension and contact angle from the shapes of axisymmetric fluid interfaces. Journal of colloid and interface science. 1983;93(1):169–183.
[154] de Gennes PG, Brochard-Wyart F, Quere D. Capillarity and Wetting Phenomena. Springer; 2004.
[155] Alvarez NJ, Walker LM, Anna SL. A non-gradient based algorithm for the determination of surface tension from a pendant drop: Application to low Bond number drop shapes. Journal of colloid and interface science. 2009;333(2):557–562.
[156] Andreas J, Hauser E, Tucker W. Boundary tension by pendant drops. The Journal of Physical Chemistry. 1938;42(8):1001–1019.
[157] Juuza J. The pendant drop method of surface tension measurement: equation interpolating the shape factor tables for several selected planes. Czechoslovak Journal of Physics. 1997;47(3):351–357.
[158] Stauffer CE. The measurement of surface tension by the pendant drop technique. The journal of physical chemistry. 1965;69(6):1933–1938.
[159] Neeson MJ, Chan DY, Tabor RF. Compound pendant drop tensiometry for interfacial tension measurement at zero Bond number. Langmuir. 2014;30(51):15388–15391.
[160] Buzzacchi M, Schmiedel P, von Rybinski W. Dynamic surface tension of surfactant systems and its relation to foam formation and liquid film drainage on solid surfaces. Colloids and Surfaces A: Physicochemical and Engineering Aspects. 2006;273(1-3):47–54.
[161] Gurkov TD, Basheva ES. Hydrodynamic behaviour and stability of approaching deformable drops. Encyclopedia of surface and colloid science. 2002;1:2349–2363.
[162] Fainerman V, Miller R. The maximum bubble pressure tensiometry. In: Studies in Interface Science. vol. 6. Elsevier; 1998. p. 279–326.
[163] Bendure RL. Dynamic surface tension determination with the maximum bubble pressure method. Journal of Colloid and Interface Science. 1971;35(2):238–248.
[164] Javadi A, Kragel J, Makievski AV, Kovalchuk VI, Kovalchuk NM, Mucic N, et al. Fast dynamic interfacial tension measurements and dilational rheology of interfacial layers by using the capillary pressure technique. Colloids and Surfaces A: Physicochemical and Engineering Aspects. 2012;407:159 – 168.
[165] Alvarez N, Walker L, Anna S. A Microtensiometer To Probe the Effect of Radius of Curvature on Surfactant Transport to a Spherical Interface. Langmuir. 2010 08;26:13310–13319.
[166] Kazakov V, Fainerman VB, Kondratenko PG, Elin AF, Sinyachenko OV, Miller R. Dilational rheology of serum albumin and blood serum solutions as studied by oscillating drop tensiometry. Colloids and surfaces B, Biointerfaces. 2008 04;62:77–82.
[167] Manga M, Hunter T, Cayre O, York D, Reichert M, Anna S, et al. Measurements of Submicron Particle Adsorption and Particle Film Elasticity at Oil-Water Interfaces. Langmuir : the ACS journal of surfaces and colloids. 2016 04;32.
[168] Alvarez NJ, Anna SL, Saigal T, Tilton RD, Walker LM. Interfacial dynamics and rheology of polymer-grafted nanoparticles at air–water and xylene–water interfaces. Langmuir. 2012;28(21):8052–8063.
[169] Russev S, Alexandrov N, Marinova K, Danov K, Denkov N, Lyutov L, et al. Instrument and methods for surface dilatational rheology measurements. The Review of scientific instruments. 2008 11;79:104102.
[170] Liggieri L, Attolini V, Ferrari M, Ravera F. Measurement of the surface dilational viscoelasticity of adsorbed layers with a capillary pressure tensiometer. Journal of colloid and interface science. 2002;255(2):225–235.
[171] Ravera F, Loglio G, Kovalchuk VI. Interfacial dilational rheology by oscillating bubble/drop methods. Current Opinion in Colloid & Interface Science. 2010;15(4):217 – 228.
[172] Narayan S, Moravec DB, Hauser BG, Dallas AJ, Dutcher CS. Removing Water from Diesel Fuel: Understanding the Impact of Droplet Size on Dynamic Interfacial Tension of Water-in-Fuel Emulsions. Energy & Fuels. 2018;32(7):7326–7337.
[173] Chen Y, Dutcher CS. Size dependent droplet interfacial tension and surfactant transport in liquid-liquid systems, with applications in shipboard oily bilgewater emulsions. Soft Matter. 2020;16:2994–3004.
[174] Pepicelli M, Jaensson N, TregouÃ«t C, Schroyen B, Alicke A, Tervoort T, et al. Surface viscoelasticity in model polymer multilayers: From planar interfaces to rising bubbles. Journal of Rheology. 2019;63(5):815–828.
[175] Freer EM, Radke CJ. Relaxation of asphaltenes at the toluene/water interface: diffusion exchange and surface rearrangement. The Journal of Adhesion. 2004;80:481–496.
[176] Loglio G, Pandolfini P, Miller R, Makievski AV, KrÃ€gel J, Ravera F, et al. Perturbation-response relationship in liq-

uid interfacial systems: non-linearity assessment by frequency-domain analysis. Colloids and Surfaces A: Physicochemical and Engineering Aspects. 2005;261(1):57 – 63.

[177] Grassia P, Neethling S, Cilliers J. Foam drainage on a sloping weir. The European Physical Journal E. 2002;8(1):517–529.

[178] Stevenson P. The wetness of a rising foam. Industrial & engineering chemistry research. 2006;45(2):803–807.

[179] de Vries AS, Wit K, et al. Rheology of gas/water foam in the quality range relevant to steam foam. SPE Reservoir Engineering. 1990;5(02):185–192.

[180] Simjoo M, Rezaei T, Andrianov A, Zitha P. Foam stability in the presence of oil: effect of surfactant concentration and oil type. Colloids and Surfaces A: Physicochemical and Engineering Aspects. 2013;438:148–158.

[181] Binks B, Davies C, Fletcher P, Sharp E. Non-aqueous foams in lubricating oil systems. Colloids and Surfaces A: Physicochemical and Engineering Aspects. 2010;360(1-3):198–204.

[182] Bhamla MS, Giacomin CE, Balemans C, Fuller GG. Influence of interfacial rheology on drainage from curved surfaces. Soft Matter. 2014;10(36):6917–6925.

[183] Garrett PR. The effect of polytetrafluoroethylene particles on the foamability of aqueous surfactant solutions. Journal of colloid and interface science. 1979;69(1):107–121.

[184] Langevin D. Influence of interfacial rheology on foam and emulsion properties. Advances in Colloid and Interface Science. 2000;88(1-2):209–222.

[185] Tuinier R, Bisperink CG, van den Berg C, Prins A. Transient foaming behavior of aqueous alcohol solutions as related to their dilational surface properties. Journal of colloid and interface science. 1996;179(2):327–334.

[186] Lorenceau E, Rouyer F. Lifetime of a single bubble on the surface of a water and ethanol bath. Physical Review Fluids. 2020;5(6):063603.

[187] Shi X, Fuller GG, Shaqfeh ES. Oscillatory spontaneous dimpling in evaporating curved thin films. Journal of Fluid Mechanics. 2020;889.

[188] Velev OD, Gurkov TD, Borwankar RP. Spontaneous cyclic dimpling in emulsion films due to surfactant mass transfer between the phases. Journal of colloid and interface science. 1993;159:497–497.

[189] Müller F, Kornek U, Stannarius R. Experimental study of the bursting of inviscid bubbles. Physical Review E. 2007;75(6):065302.

[190] Pandit A, Davidson J. Hydrodynamics of the rupture of thin liquid films. Journal of Fluid Mechanics. 1990;212:11–24.

[191] Müller F, Stannarius R. Comparison of the rupture dynamics of smectic bubbles and soap bubbles. Liquid Crystals. 2009;36(2):133–145.

[192] Robinson ND, Steen PH. Observations of singularity formation during the capillary collapse and bubble pinch-off of a soap film bridge. Journal of colloid and interface science. 2001;241(2):448–458.

[193] Tammaro D, Pasquino R, Villone MM, D'Avino G, Ferraro V, Di Maio E, et al. Elasticity in bubble rupture. Langmuir. 2018;34(19):5646–5654.

[194] Sabadini E, Ungarato RF, Miranda PB. The elasticity of soap bubbles containing wormlike micelles. Langmuir. 2014;30(3):727–732.

[195] Debrégeas Gd, De Gennes PG, Brochard-Wyart F. The life and death of" bare" viscous bubbles. Science. 1998;279(5357):1704–1707.

[196] Poulain S, Bourouiba L. Biosurfactants change the thinning of contaminated bubbles at bacteria-laden water interfaces. Physical Review Letters. 2018;121(20):204502.

[197] Bico J. Cracks in bursting soap films. Journal of Fluid Mechanics. 2015;778:1–4.

[198] De Vries A. Foam stability: Part IV. Kinetics and activation energy of film rupture. Recueil des Travaux Chimiques des Pays-Bas. 1958;77(4):383–399.

[199] Langevin D. Coalescence in foams and emulsions: Similarities and differences. Current Opinion in Colloid & Interface Science. 2019;44:23 – 31. Memorial Volume.

[200] Hildebrand JH. Emulsion Type. The Journal of Physical Chemistry. 1941;45(8):1303–1305.

[201] Traykov TT, Manev ED, Ivanov IB. Hydrodynamics of thin liquid films. Experimental investigation of the effect of surfactants on the drainage of emulsion films. International Journal of Multiphase Flow. 1977;3(5):485 – 494.

[202] Ivanov IB, Kralchevsky PA. Stability of emulsions under equilibrium and dynamic conditions. Colloids and surfaces A, Physicochemical and engineering aspects. 1997;128(1-3):155–175.

[203] Pickering SU. Cxcvi.—Emulsions. Journal of the Chemical Society, Transactions. 1907;91:2001–2021.

[204] Du Sorbier QM, Aimable A, Pagnoux C. Influence of the electrostatic interactions in a Pickering emulsion polymerization for the synthesis of silica–polystyrene hybrid nanoparticles. Journal of colloid and interface science. 2015;448:306–314.

[205] Menon V, Wasan D. Characterization of oil—water interfaces containing finely divided solids with applications to the coalescence of water-in-oil Emulsions: A review. Colloids and surfaces. 1988;29(1):7–27.

[206] Binks BP, Clint JH. Solid wettability from surface energy components: relevance to Pickering emulsions. Langmuir. 2002;18(4):1270–1273.

[207] Aveyard R, Binks BP, Clint JH. Emulsions stabilised solely by colloidal particles. Advances in Colloid and Interface Science. 2003;100:503–546.

[208] Yang Y, Fang Z, Chen X, Zhang W, Xie Y, Chen Y, et al. An overview of Pickering emulsions: solid-particle materials, classification, morphology, and applications. Frontiers in pharmacology. 2017;8:287.

[209] Chen W, Liu X, Liu Y, Kim HI. Novel synthesis of self-assembled CNT microcapsules by O/W Pickering emulsions. Materials Letters. 2010;64(23):2589–2592.

[210] Williams M, Olland B, Armes SP, Verstraete P, Smets J. Inorganic/organic hybrid microcapsules: Melamine formaldehyde-coated Laponite-based Pickering emulsions. Journal of colloid and interface science. 2015;460:71–80.

[211] Frelichowska J, Bolzinger MA, Valour JP, Mouaziz H, Pelletier J, Chevalier Y. Pickering w/o emulsions: drug release and topical delivery. International journal of pharmaceutics. 2009;368(1-2):7–15.

[212] Kashchiev D, Exerowa D. Nucleation mechanism of rupture of Newtonian black films. I. Theory. Journal of Colloid and Interface Science. 1980;77(2):501–511.

[213] Kabalnov A, Wennerström H. Macroemulsion stability: the oriented wedge theory revisited. Langmuir. 1996;12(2):276–292.

[214] de Gennes PG. Some remarks on coalescence in emulsions or foams. Chemical engineering science. 2001;56(19):5449–5450.

[215] Frostad J, Walter J, Leal L. A scaling relation for the capillary-pressure driven drainage of thin films. Physics of Fluids. 2013;25(5):052108.

[216] Kavehpour HP. Coalescence of drops. Annual Review of Fluid Mechanics. 2015;47:245–268.

[217] Fullana JM, Zaleski S. Stability of a growing end rim in a liquid sheet of uniform thickness. Physics of Fluids. 1999;11(5):952–954.

[218] Menchaca-Rocha A, Martínez-Dávalos A, Nunez R, Popinet S, Zaleski S. Coalescence of liquid drops by surface tension. Physical Review E. 2001;63(4):046309.

[219] Duchemin L, Eggers J, Josserand C. Inviscid coalescence of drops. arXiv preprint physics/0212075. 2002;.
[220] Aarts DG, Lekkerkerker HN, Guo H, Wegdam GH, Bonn D. Hydrodynamics of droplet coalescence. Physical review letters. 2005;95(16):164503.
[221] Thoroddsen S, Takehara K, Etoh T. The coalescence speed of a pendent and a sessile drop. Journal of Fluid Mechanics. 2005;527:85.
[222] Aryafar H, Lukyanets A, Kavehpour H. Inertia-dominated coalescence of drops. Applied Mathematics Research eXpress. 2006;2006.
[223] Eggers J, Lister JR, Stone HA. Coalescence of liquid drops. Journal of Fluid Mechanics. 1999;401:293–310.
[224] Zhang Q, Jiang X, Brunello D, Fu T, Zhu C, Ma Y, et al. Initial coalescence of a drop at a planar liquid surface. Physical Review E. 2019;100(3):033112.
[225] Aryafar H, Kavehpour H. Hydrodynamic instabilities of viscous coalescing droplets. Physical Review E. 2008;78(3):037302.
[226] De Malmazet E, Risso F, Masbernat O, Pauchard V. Coalescence of contaminated water drops at an oil/water interface: Influence of micro-particles. Colloids and Surfaces A: Physicochemical and Engineering Aspects. 2015;482:514–528.